NUCLEAR FORENSICS METHODOLOGY FOR SOURCE REACTOR-TYPE DISCRIMINATION OF CHEMICALLY SEPARATED PLUTONIUM

A Dissertation

by

JEREMY MICHAEL OSBORN

Submitted to the Office of Graduate and Professional Studies of
Texas A&M University
in partial fulfillment of the requirements for the degree of

DOCTOR OF PHILOSOPHY

Chair of Committee,	Sunil S. Chirayath
Committee Members,	Craig M. Marianno
	Marvin L. Adams
	Charles M. Folden III
Head of Department,	Yassin A. Hassan

December 2018

Major Subject: Nuclear Engineering

ABSTRACT

The growing nuclear threat has heightened the need for developing nuclear forensics analysis techniques that contribute to nuclear material source attribution, thereby strengthening nuclear deterrence. The objective of this research was to develop a nuclear forensics methodology that is capable of source reactor-type discrimination of chemically separated weapons-usable plutonium. The developed methodology utilizes plutonium and fission product intra-element isotope ratios within the plutonium sample to predict characteristics of the irradiated material, including burnup, time since irradiation, and reactor type.

The MCNPX-2.7 and MCNP6 radiation transport codes were used to model reactor cores, perform burnup simulations, and estimate the isotopics of the discharged fuel. Ratios of intra-element isotopes (fission products and plutonium) were identified which contribute to resolving the parameters of burnup, time since irradiation, and reactor type. The simulation results were used to generate a reactor-dependent library of intra-element isotope ratio values as a function of burnup and time since irradiation. A maximum likelihood calculation was utilized to compare the simulated intra-element isotope ratio values contained in the reactor library to the same ratio values measured in the sample. The result is a likelihood value which is proportional to the probability of observing the measured intra-element isotope ratios given the reactor type and parameters.

In order to validate the nuclear forensics methodology developed, two experimental irradiation campaigns were performed, resulting in two distinct UO_2 fuel samples containing weapons-usable plutonium. The first was designed to replicate weapons-usable plutonium produced in the blanket of a fast breeder reactor, by irradiating depleted UO_2 fuel samples in a pseudo-fast neutron spectrum within the High Flux Isotope Reactor at Oak Ridge National Laboratory. The second irradiation was designed to represent weapons-usable plutonium produced in a natural uranium fueled thermal reactor, by irradiating natural UO_2 fuel samples in a thermal neutron spectrum at the University of Missouri Research Reactor. The irradiated samples were subjected to nondestructive and destructive analyses to measure the plutonium and fission product isotope ratios. The methodology performed well for both experimentally irradiated cases, identifying the source reactor model and adequately predicting the burnup and time since irradiation. The work presented here served to develop and validate a nuclear forensics source reactor-type discrimination methodology.

ACKNOWLEDGEMENTS

I would like to thank my advisor, Dr. Sunil Chirayath for all the years of his guidance and care. Dr. Chirayath constantly goes above and beyond for his students, and I am fortunate to have such a mentor. I would also like to thank the rest of my committee members, Dr. Marianno, Dr. Adams, and Dr. Folden. All four committee members have made significant impacts on my academic career, and I am proud to have their names on this dissertation.

Thanks also go to the members of our nuclear forensics research group meeting, Dr. Chirayath, Dr. Folden, Dr. Evans Kitcher, Dr. Jonathan Burns, and Kevin Glennon, for their weekly direction and influence.

Thank you to my parents, Sean and Amy, for their endless amounts of support and encouragement. Finally, I must thank my wife, Noel, for her patience and love.

CONTRIBUTORS AND FUNDING SOURCES

Contributors

This work was supported by a dissertation committee consisting of Professors Sunil S. Chirayath, Craig M. Marianno and Marvin L. Adams of the Department of Nuclear Engineering and Professor Charles M. Folden III of the Department of Chemistry.

The cation exchange column chromatography, mass spectrometry sample preparation, and mass spectrometry analyses depicted in Section 5.2 and Section 7.3 were conducted by Kevin Glennon of the Department of Chemistry.

All other work conducted for the dissertation was completed by the student independently.

Funding Sources

This work was made possible by the U.S. Department of Homeland Security, Domestic Nuclear Detection Office under Grant Numbers: NSF Grant No. ECCS-1140018, DHS-2012-DN-077-ARI1057-02&03, and DHS-2015-DN-077-ARI1099.

The contributions from Kevin Glennon were made possible by the Department of Energy National Nuclear Security Administration through the Nuclear Science and Security Consortium under Award Number(s) DE-NA0003180 and/or DE-NA0000979.

Its contents are solely the responsibility of the author and do not necessarily represent the official views of the U.S. Department of Homeland Security, Domestic

Nuclear Detection Office or the Department of Energy National Nuclear Security Administration.

TABLE OF CONTENTS

Page

LIST OF FIGURES

Page

LIST OF TABLES

Page

1. INTRODUCTION

The 2018 Nuclear Posture Review[1] reiterates that nuclear terrorism remains among the most significant threats to the United States with the most dangerous being an improvised nuclear device (IND). An aspect of combatting this threat includes technical nuclear forensics and attribution capabilities as a deterrent to state support of nuclear terrorism.[1] Attribution consists of nuclear and traditional forensic evaluations, and is the process by which interdicted, illicit nuclear material is analyzed in order to identify its location of origin and production source.[2]

The research presented here is motivated by the hypothetical situation of an interdiction of weapons-usable plutonium material which would be suitable for use in an IND. The weapons-usable plutonium could have resulted from plutonium leaving safeguards or plutonium which was produced outside of safeguards. Typically, the International Atomic Energy Agency (IAEA) would monitor such plutonium through safeguards agreements with countries. However, there are cases of plutonium production occurring in states where nuclear fuel cycle facilities are not under IAEA safeguards.[3]

In an article by M. Miller, three aspects were considered where an attribution capability may deter state support of nuclear terrorism.[4]

(1) Nuclear attribution may deter a rational government from clandestinely supplying nuclear material to terrorists.[4]

(2) A state may improve the security of its nuclear weapons and material out of fear of attribution and accountability for any material becoming out of regulatory control from the facility.[4]

(3) A rogue actor within a state may be deterred from providing technical assistance to a terrorist if it is known that the material source will be identified.[4]

The Pelindaba Nuclear Facility is South Africa's main nuclear research center and houses hundreds of kilograms of highly-enriched uranium (HEU) remaining from South Africa's nuclear weapons program. On November 8, 2007 the Pelindaba facility was breached by two teams of unidentified armed assailants.[5] More concerning is the possibility that the assailants may have benefited from insider support, and the lack of response from the South African government. The security breach at Pelindaba confirms that the nuclear terrorism threat is real. Moreover, it highlights the need for a credible nuclear forensics capability to deter such a lax security environment from a country possessing weapons-usable nuclear material.

A boon to technical nuclear forensics efforts is the fact that all plutonium samples of interest to nuclear forensics originate within nuclear reactors.[6] The weapons-desirable plutonium isotope, ^{239}Pu is produced during the operation of a nuclear reactor by a neutron capture reaction on the uranium isotope ^{238}U followed by two successive beta decays. As reactor operation continues and fuel burnup increases, (fuel burnup being defined as the thermal energy produced per unit mass of fuel and expressed in units of gigawatt-days per metric ton of uranium [GWd/MTU]), subsequent neutron reactions on ^{239}Pu lead to the production of a full suite of plutonium isotopes known as the plutonium vector (^{238}Pu, ^{239}Pu, ^{240}Pu, ^{241}Pu, and ^{242}Pu,). It is understood that weapons-grade plutonium (~94% ^{239}Pu) will be produced if uranium is subject to low

levels of fuel burnup (< 5 GWd/MTU).[7] It follows that because plutonium is produced during the operation of a nuclear reactor, there may be characteristics of the irradiated plutonium material that contain indigenous information on the source reactor and operation parameters. This information can provide a capability for reactor-type discrimination and possibly source attribution of plutonium.

The objective of this research was to develop, verify, and validate a nuclear forensics methodology that is capable of source reactor-type discrimination of chemically separated weapons-usable plutonium. In the event of plutonium interdiction, the reactor-type discrimination methodology may be combined with additional forensic evidence to contribute to the source attribution of the plutonium. To demonstrate the methodology two experimental irradiation campaigns of uranium surrogates (depleted UO_2 and natural UO_2) were performed at the High Flux Isotope Reactor (HFIR) and the University of Missouri Research Reactor (MURR), respectively, for the purpose of producing small quantities (< 1mg) of weapons-usable plutonium test material.

1.1 Previous Nuclear Forensics Studies

Traditional nuclear forensics techniques exploit the known production and loss mechanisms of isotopes in irradiated fuel, as well as radioactive decay, in order to relate actinide and fission product isotopic concentrations to parameters of interest. Multiple studies have been published detailing nuclear forensics capabilities which can predict parameters such as initial uranium enrichment of the irradiated fuel, level of fuel burnup, age of the material, and the source reactor type from isotopic concentrations.[8,9,10,11,12,13,14] These techniques are applied to spent (used) fuel material and require a knowledge of

the isotopic concentrations in the unprocessed fuel material. However, in the event of a plutonium interdiction, chemical separation of the plutonium cannot be dismissed. Once a chemical actinide separation has occurred that knowledge of the original isotopic concentrations is lost.

If the degree of purification achieved by a separation process can be assumed, previous research has demonstrated an ability of plutonium and trace fission product contaminant isotopes for use in source discrimination of a fast or thermal reactor type.[10,14] The potential for the presence of trace amounts of fission products in chemically separated plutonium is due to the use of a non-ideal purification process. The degree of purification achieved by a separation process can be quantified by decontamination factors (DF), which are the ratios of a stated impurity to a desired component in the feed divided by the equivalent ratio in the product.[15]

$$DF = \frac{[\frac{Impurity}{Desired\ Component}]_{Feed}}{[\frac{Impurity}{Desired\ Component}]_{Product}} \quad (1)$$

The most commonly employed technique for plutonium separation from irradiated nuclear fuel is the Plutonium Uranium Redox EXtraction (PUREX) process.[16] A study by P.M. Mendoza showed that for plutonium separated by PUREX the elemental decontamination factors vary drastically between elements and are a strong function of the separation process parameters.[17] Predicting an amount of isotope separation will be unrealistic without knowledge of the specific process parameters. In response to the possibility of the plutonium having undergone a chemical actinide separation process, intra-element isotope ratios may be employed as forensics signatures.

Since isotopes of an element will have the same decontamination factor, forensics signatures comprised of intra-element isotope ratios will retain their information regardless of chemical process or efficiency.

1.2 Basis for Current Research

Studies by I. Lantzos[18] and A. Glaser[19] utilized only the plutonium isotope ratios for discriminating amongst reactor types. Lantzos used the ORIGEN-ARP depletion module contained within the SCALE6.1 package[20] to generate plutonium isotopics for multiple reactor types and multiple initial fuel enrichments. The reactor types analyzed included fuels typically discharged from a Pressurized Water Reactor (PWR), Boiling Water Reactor (BWR), and Liquid Metal Fast Breeder Reactor (LMFBR). Fuel burnup simulations of the spent fuel ranged from 25-45 GWd/MTU for the light water reactors (PWR and BWR) and 60-100 GWd/MTU for the LMFBR. By plotting the spent fuel isotopics as a function of three plutonium isotope ratios ($^{239}Pu/^{240}Pu$, $^{242}Pu/^{240}Pu$, and $^{238}Pu/Pu_{Total}$) an observable distinction occurred in the grouping of the light water reactors and the LMFBR. However, this distinction will be significantly reduced when analyzing the irradiated fuel at a low burnup conducive to weapons-usable plutonium production. The study by Glaser[19] again utilizes plutonium isotope ratios for reactor-type discrimination, but with a focus on weapons-grade plutonium. MCNP[21] and ORIGEN2[22] were used for neutronics and depletion calculations for a Hanford-type, NRX-type, and Calder Hall-type reactor. These three reactor types are all thermal reactors fueled with natural uranium and have historically been used for plutonium production. For each reactor type, the plutonium composition was obtained and ratios of plutonium isotopes

were analyzed. It was found that even for increasing levels of burnup, and decreasing ^{239}Pu fraction to approximately 90%, the composition of the plutonium vectors are remarkably similar amongst the three production reactor types. When differing reactor types were added including a low-enriched PWR and fast breeder reactor (FBR) an observable difference occurred in the grouping of these plutonium isotope ratios.

A forensics methodology comprised of predictive ratios of plutonium isotopes has the benefit of being independent of chemical separation. However, including intra-element ratios of fission products in the methodology may aid in discriminating between reactors with similar neutron spectra, a weakness in an approach purely utilizing the plutonium vector. Additionally, the methodology could be improved by incorporating a way to quantify how similar a measured sample is to a predicted reactor type, rather than observation by grouping.

A verification technique for use at spent fuel reprocessing facilities was developed by W. Charlton *et al.* which involved measurements of isotopic ratios of noble fission product gasses.[23] The four intra-element isotope ratios, comprised of krypton and xenon fission products, have the ability to predict parameters such as fuel burnup and reactor type. Reactor analysis codes were used to create a database of krypton and xenon isotopic ratios as a function of fuel burnup for various reactor types. The technique developed uses a high-precision isotope mass spectrometer to measure stable noble gas isotope compositions in samples taken from a reprocessing plant exhaust stack. The measured isotopic ratios are compared to a database of isotopic ratios to infer the fuel parameters. The comparison performed utilized a Bayesian analysis

technique which calculated the probability, given a reactor model and burnup, of observing the measured isotopic ratios.

The technique developed by Charlton *et al.* exploits the fact that noble gases are not chemically bound to the fuel and are thus released during reprocessing. While the krypton and xenon intra-element isotope ratios identified are not useful for analyzing post-processed materials, the work demonstrated the ability for fission product intra-element ratios to contain information capable of inferring critical parameters such as fuel burnup and reactor type. Additionally, the Bayesian analysis technique used provided a basis for quantifying the comparison of a set of measured isotopic ratios to a reactor-dependent database. For the research presented hereafter we envision a technique similar to those developed by Glaser[19] and Charlton[23] that can be expanded for the source reactor-type discrimination of chemically separated weapons-usable plutonium based upon intra-element isotope ratios of plutonium and fission product contaminants.

2. FORENSICS METHODOLOGY AND DEVELOPMENT*

If special nuclear material is interdicted, a few steps may be followed leading to the utilization of the methodology developed through this study. The first step will be to perform a gamma spectrometry measurement to ascertain whether the material contains plutonium. Next, a sample will be drawn to perform precise gamma and mass spectrometry measurements to obtain as many fission product and plutonium intra-element isotope ratios as possible. Subsequently, the measured intra-element isotope ratios can be utilized in the nuclear forensics methodology for discriminating against reactor types not likely of being the source of the interdicted material. The information gained by the reactor-type discrimination methodology, when combined with traditional forensics, may enable attribution of the plutonium.

The reactor-type discrimination methodology developed utilizes a library comparison employing a maximum likelihood calculation in which a set of measured intra-element isotope ratio values from an unknown irradiation are compared to a reactor-dependent library of the same ratio values created through computational burnup and decay simulations. For isotopes having short-lived precursors, at each burn step in the reactor-dependent library the short-lived precursors were summed with the isotope of interest. This allows the ratio values, as a function of burnup, to be representative of a measured value at a later measurement date assuming the precursors have completely

* Reprinted with permission from "Nuclear Forensics Methodology for Reactor-Type Attribution of Chemically Separated Plutonium" by J.M. Osborn *et al.*, 2017. *Nucl. Tech.*, 201, 1-10, Copyright 2017 by American Nuclear Society.

decayed during some minimum reprocessing time. The description of the creation of the reactor-dependent library which consists of intra-element isotope ratio values as a function of burnup and time since irradiation is described in Section 3.4.

2.1 Intra-Element Isotope Ratio Identification

The objective of this research was to develop a nuclear forensics methodology for the source reactor-type discrimination of weapons-useable plutonium, in the event of a plutonium interdiction. Due to the possibility of a chemical actinide separation prior to interdiction, intra-element isotope ratio values rather than isotope concentrations, were required as characteristic signatures. In addition to identifying the most likely source reactor from the library of reactors, it is was desired to reconstruct reactor parameter conditions corresponding to the interdicted material. These parameters could include burnup, time since irradiation ended, initial fuel enrichment, power level, operating history, etc. Any parameter which has an effect on the irradiated fuel isotopics could theoretically be resolved with identification and inclusion of the appropriate isotopic ratios. The reactor parameters pursued in this study are burnup, time since irradiation, and reactor type. In order to downselect from all the isotopes available from an MCNP burnup simulation to a set of ratios, a number of factors were considered. Foremost, multiple isotopes of the same element must be produced in the irradiated fuel as well as being produced in significant quantities to be reported in MCNP simulation outputs. The isotopes must also have sufficiently long half-lives (greater than 1 y), and be produced in a sufficient amount to allow measurement of the ratio within a chemically processed sample (greater than 1 mg of isotope per 1 kg of plutonium, i.e. 1 ppm). Finally, either

the production or decay of the isotope ratio must have a functional dependence on at least one of the parameters of interest. The functional form criteria is the most important when identifying isotope ratios, as this will lead to the resolution of parameters. Thus, the value of an intra-element isotope ratio must change; (1) as a function of burnup, (2) based on the reactor type, or (3) as a function of time since irradiation due to the decay of at least one of the isotopes in the ratio. Based on the criteria described above several intra-element ratios were analyzed for various functional dependence on the reactor parameters of interest. From the analysis the following isotope ratios were selected for the methodology to predict the reactor parameters of interest: $^{137}Cs/^{133}Cs$, $^{134}Cs/^{137}Cs$, $^{135}Cs/^{137}Cs$, $^{136}Ba/^{138}Ba$, $^{150}Sm/^{149}Sm$, $^{152}Sm/^{149}Sm$, $^{154}Eu/^{153}Eu$, $^{240}Pu/^{239}Pu$, $^{241}Pu/^{239}Pu$, and $^{242}Pu/^{239}Pu$.

In traditional nuclear forensic techniques the concentration of ^{137}Cs ($^{137}Cs/U$) is a well-known burnup monitor. ^{137}Cs is a direct fission product with a high fission yield (~6.5%), which is relatively independent of fissile isotope and incident neutron energy. The loss mechanisms of decay and neutron capture for ^{137}Cs are insignificant due to a long half-life and low neutron capture cross section, respectively. On decay the 661.7 keV gamma ray is easily measurable. These attributes lead to the ratio of $^{137}Cs/U$ increasing linearly with burnup, making $^{137}Cs/U$ an ideal monitor for estimating burnup. Conversely, ^{133}Cs is not known as a burnup monitor, likely due to it being stable. However, the production and loss mechanisms of ^{133}Cs are similar to those of ^{137}Cs, with the exception of decay. If stable isotopes were to be measured using mass spectrometry then the same attributes making the $^{137}Cs/U$ ratio a useful burnup monitor will also make

the ^{133}Cs/U ratio a suitable monitor for estimating burnup. These well-known properties of isotopic concentrations can be counterintuitive when employing intra-element isotope ratios. The concentration behavior of both ^{137}Cs and ^{133}Cs contain information on burnup, but the intra-element ratio of ^{137}Cs/^{133}Cs negates the burnup dependence. Both ^{137}Cs and ^{133}Cs are produced with similar fission yields and have insignificant dependence on neutron energy. Assuming the irradiation or shutdown times are not large compared to the half-life of ^{137}Cs, this leads to the ratio quickly approaching an asymptotic value close to 1 with almost no dependence on burnup or reactor type. The MCNP calculated ratio values of ^{137}Cs/^{133}Cs are shown in Fig. 1 as a function of burnup for the commercial reactor types in the reactor library. This behavior is quite useful when paired with isotopic decay. The isotope ^{133}Cs is stable while ^{137}Cs is radioactive, resulting in the ^{137}Cs/^{133}Cs ratio value decaying with a half-life of 30.08 y. With the ^{137}Cs/^{133}Cs ratio being relatively independent of burnup and reactor type, a measured value of the ^{137}Cs/^{133}Cs ratio will indicate the time since irradiation ended for the irradiated material. The other ratios containing radioactive isotopes also contribute to determining the time since irradiation.

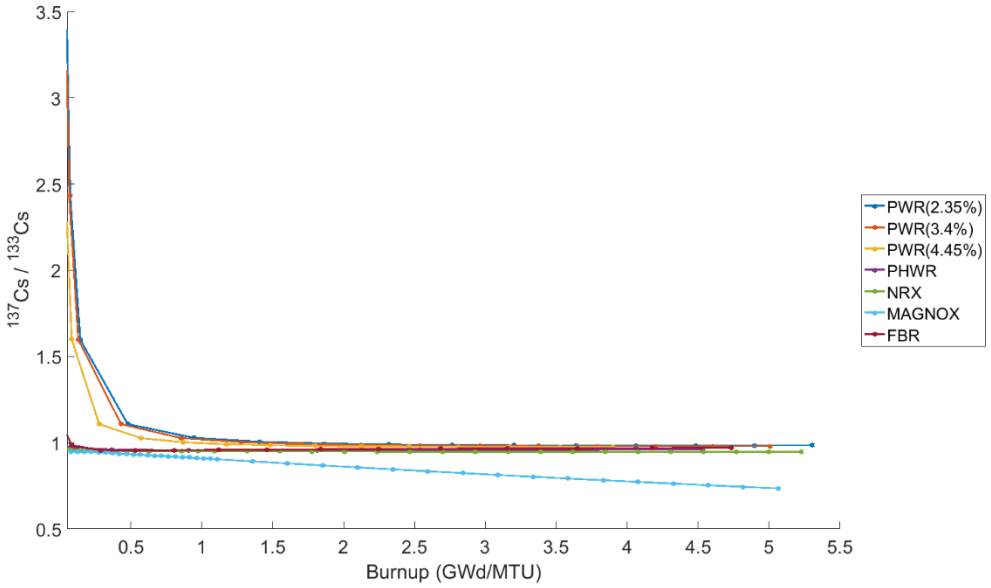

Figure 1: The $^{137}Cs/^{133}Cs$ ratio as a function of burnup.

It is evident from Fig. 1 that the $^{137}Cs/^{133}Cs$ ratio for the Magnox reactor does not follow the expected behavior. The specific Magnox reactor modeled here was the North Korea Yongbyon reactor. The Yongbyon reactor has a low power density and is designed for low burnup irradiations.[24] The simulation was carried for the fuel to reach a burnup of 5 GWd/MTU for comparison with the other reactor even though such a level of burnup is unrealistic. The low power density meant that operation had to be simulated for approximately 28 years in order to reach such a burnup. Thus the assumption made earlier regarding the irradiation time is not true for the Magnox case. This unrealistic and extended irradiation meant a significant amount of ^{137}Cs was decaying during the irradiation and the $^{137}Cs/^{133}Cs$ ratio falling below 1. Decay during the extended

irradiation of the Magnox model causes unexpected behaviors in the other intra-element isotope ratios containing a radioactive isotope as well.

The other cesium isotopes selected included ^{134}Cs and ^{135}Cs. In the mass 134 fission yield chain ^{134}Cs is blocked by stable ^{134}Xe, and the production from fission is negligible. Thus, ^{134}Cs is produced from radiative capture on ^{133}Cs. As noted, the concentration of ^{133}Cs increases linearly with burnup meaning the rate of change of ^{134}Cs increases with burnup. As a result the ^{134}Cs/^{137}Cs ratio is expected to behave fairly linearly with burnup. This behavior is generally observed in Fig. 2, excluding the Magnox, NRX, and FBR models. The half-life of ^{134}Cs is approximately 2.06 years and the long irradiation times required to simulate the Magnox, NRX, and FBR blanket materials to the selected burnup level cause the unexpected behaviors. The ^{134}Cs/^{137}Cs ratio serves to demonstrate a ratio which contributes to resolving burnup.

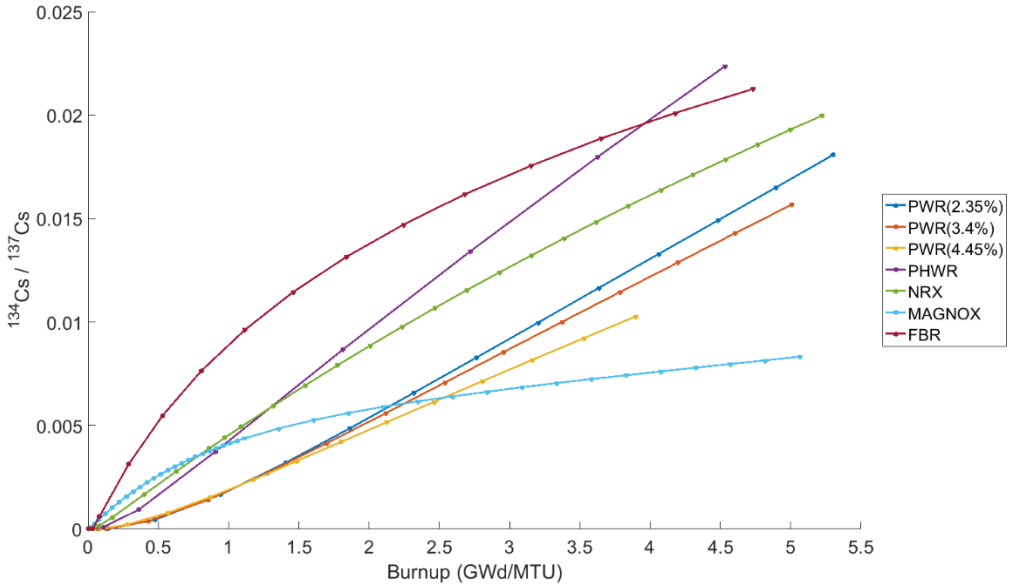

Figure 2: The $^{134}Cs/^{137}Cs$ ratio as a function of burnup.

The two main production mechanisms of ^{135}Cs are the radiative capture on ^{134}Cs and the decay of ^{135}Xe. Due to the relatively small concentration of ^{134}Cs, the production of ^{135}Cs is dominated by the decay of ^{135}Xe. As will be discussed in Section 7.1, the competition of neutron capture versus decay for ^{135}Xe results in the concentration of ^{135}Cs being inversely related to the thermal neutron flux magnitude. The loss mechanisms of stable ^{135}Cs are negligible meaning the concentration will be linear with burnup and inversely related to the thermal neutron flux magnitude. Similar to the $^{137}Cs/^{133}Cs$ ratio, with both ^{135}Cs and ^{137}Cs behaving linearly with burnup the ratio $^{135}Cs/^{137}Cs$ will reach a constant value. However, due to the behavior of ^{135}Cs the constant value of $^{135}Cs/^{137}Cs$ will be inversely related to the thermal neutron flux

magnitude. The $^{135}Cs/^{137}Cs$ ratio as a function of burnup is shown in Fig. 3 and serves to demonstrate a ratio which contributes to resolving reactor type.

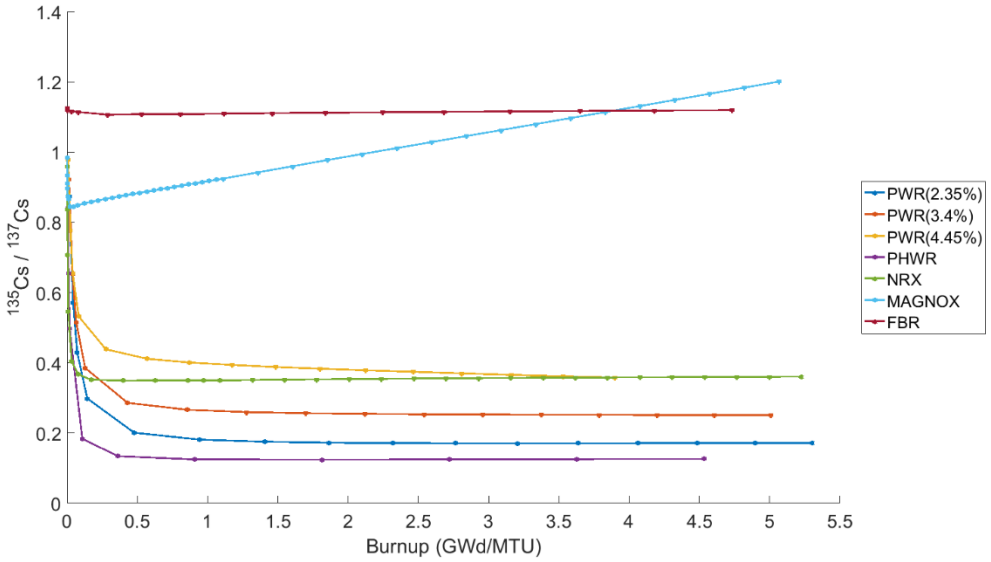

Figure 3: The $^{135}Cs/^{137}Cs$ ratio as a function of burnup.

Figure 4 displays the $^{136}Ba/^{138}Ba$ ratio as a function of burnup. The general trend is similar to that of the $^{134}Cs/^{137}Cs$ ratio, with the stable $^{136}Ba/^{138}Ba$ ratio being fairly linear with burnup, and the main distinction being the inverse relation to the thermal flux magnitude. The similarity in the ratio stems from the similar production mechanisms of the individual isotopes. Analogous with ^{137}Cs, ^{138}Ba is the stable nuclide of the mass 138 chain, and has minimal loss mechanisms resulting in the production being linear with burnup. The behavior of the concentration of ^{136}Ba is discussed in more detail in Section 7.1. The production of ^{136}Ba results from the decay of ^{136}Cs which is primarily produced

via the neutron capture on ^{135}Cs, and is thus inversely related to the thermal neutron flux magnitude.

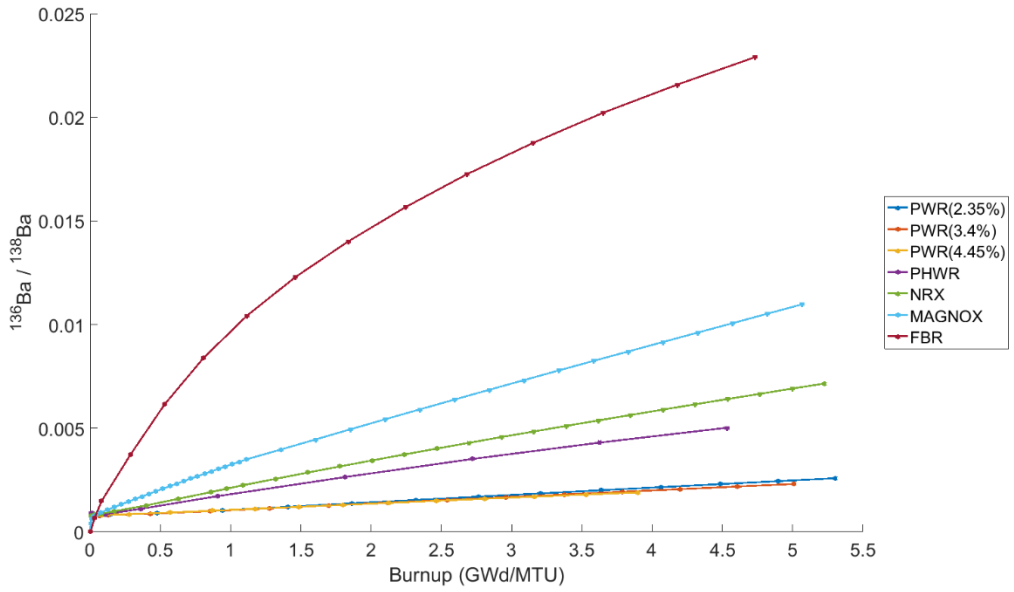

Figure 4: The $^{136}Ba/^{138}Ba$ ratio as a function of burnup.

A good example of a characteristic ratio useful for determining reactor type is $^{150}Sm/^{149}Sm$. ^{150}Sm and ^{149}Sm are stable isotopes and their ratio increases with increasing fuel burnup with a large dependency on the neutron energy spectrum. This behavior is due to the radiative capture cross-section of the well-known fission product neutron poison, ^{149}Sm, which has a large reaction cross-section for thermal neutron absorption in a reactor. The large thermal neutron capture cross-section for ^{149}Sm leads to the concentration of ^{149}Sm reaching a constant equilibrium value, while the concentration of ^{150}Sm is produced linearly with burnup and directly related to the

thermal neutron flux magnitude. Figure 5 shows the $^{150}Sm/^{149}Sm$ ratio which is produced linearly with burnup. The $^{150}Sm/^{149}Sm$ ratio is plotted on a semi-logarithmic scale in Fig. 6, as to highlight the grouping and separation of the reactor types. The $^{150}Sm/^{149}Sm$ ratio value is orders of magnitude larger in the thermal reactors than in the fast reactor, FBR, as well as separating amongst the natural uranium fueled thermal reactors and the enriched uranium fueled PWRs. The $^{152}Sm/^{149}Sm$ ratio, presented in Fig. 7, similarly has a ratio behavior which is fairly linear with burnup and directly related to the magnitude of the thermal neutron flux.

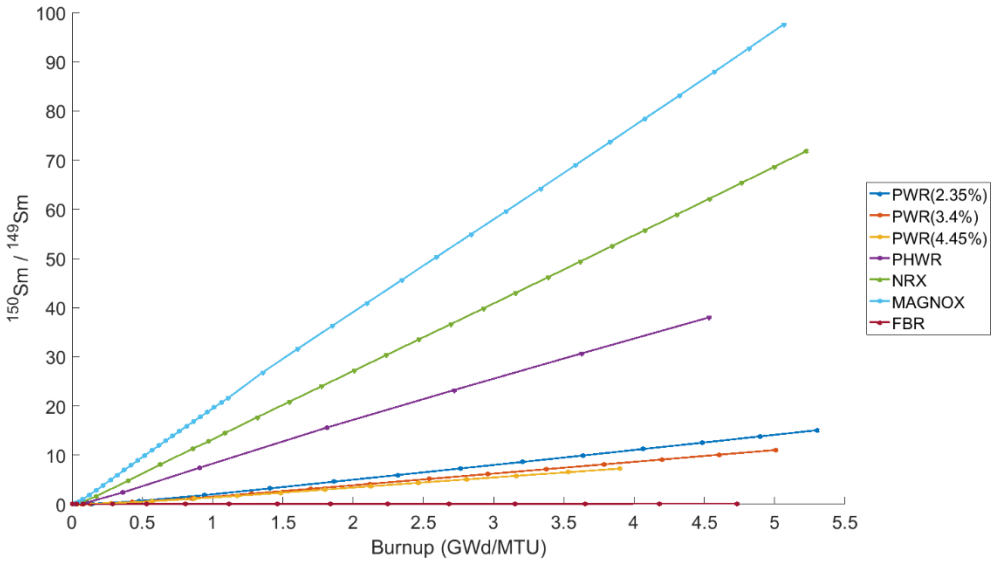

Figure 5: The $^{150}Sm/^{149}Sm$ ratio as a function of burnup.

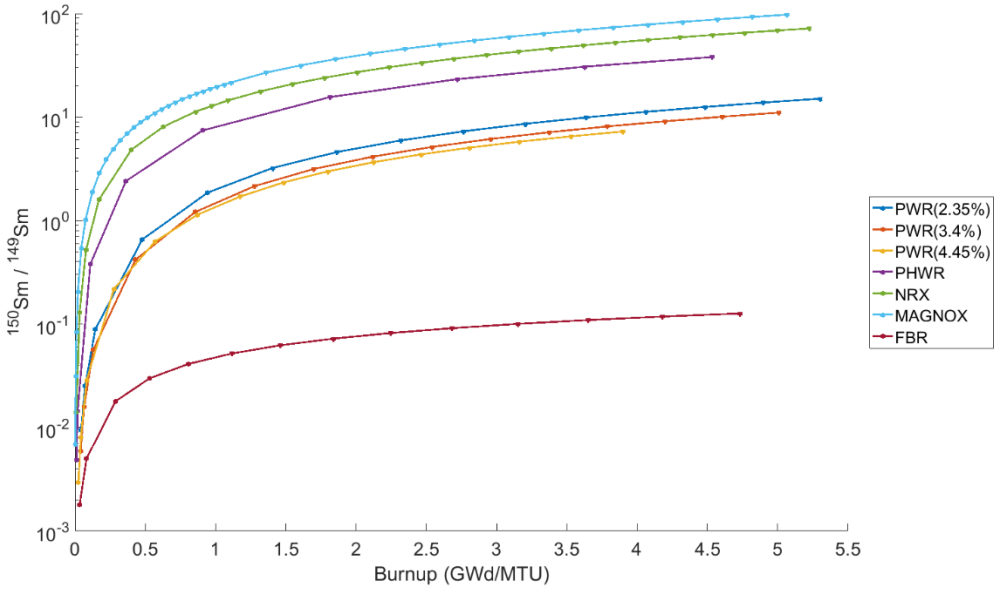

Figure 6: The ^{150}Sm/^{149}Sm ratio as a function of burnup plotted on a semi-logarithmic scale.

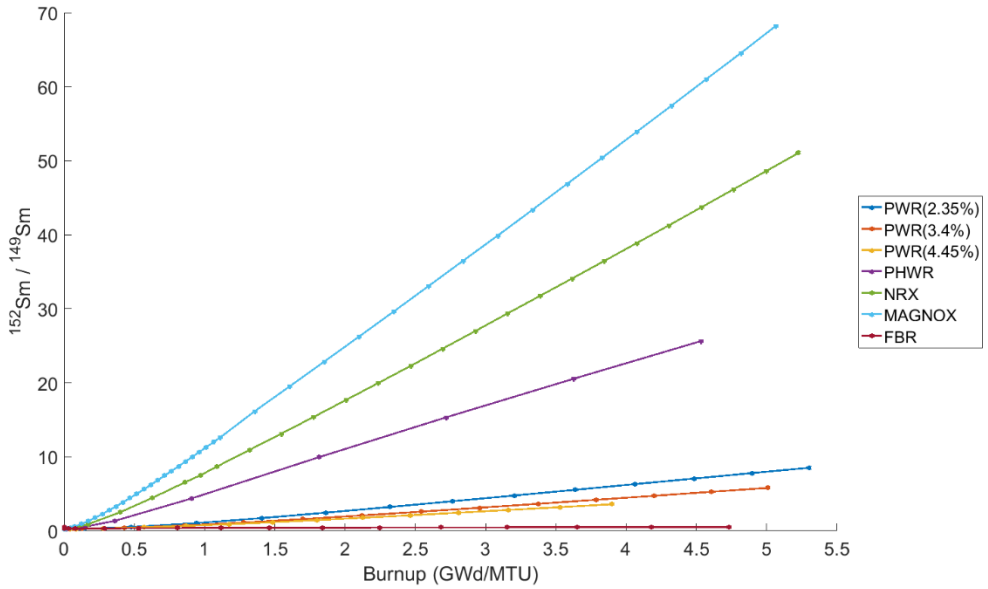

Figure 7: The ^{152}Sm/^{149}Sm ratio as a function of burnup.

As the stable nuclide of mass chain 153, ^{153}Eu is produced as a fission product and from the radiative capture on ^{152}Eu. Blocked by stable ^{154}Sm, the only significant production mechanism for ^{154}Eu is from the radiative capture on ^{153}Eu. The only loss mechanism of ^{154}Eu during irradiation, other than decay, is the radiative capture on ^{154}Eu itself. The ^{154}Eu(n,γ)^{155}Eu cross section is significantly larger than the ^{153}Eu(n,γ)^{154}Eu cross-section. At a low level of burnup the ^{154}Eu/^{153}Eu ratio, plotted in Fig. 8, is monotonically increasing with burnup. However, as burnup and the concentration of ^{154}Eu increases, the ^{154}Eu neutron capture reaction rate will approach that of the ^{153}Eu neutron capture reaction rate, and the ^{154}Eu/^{153}Eu ratio will approach an asymptotic value.

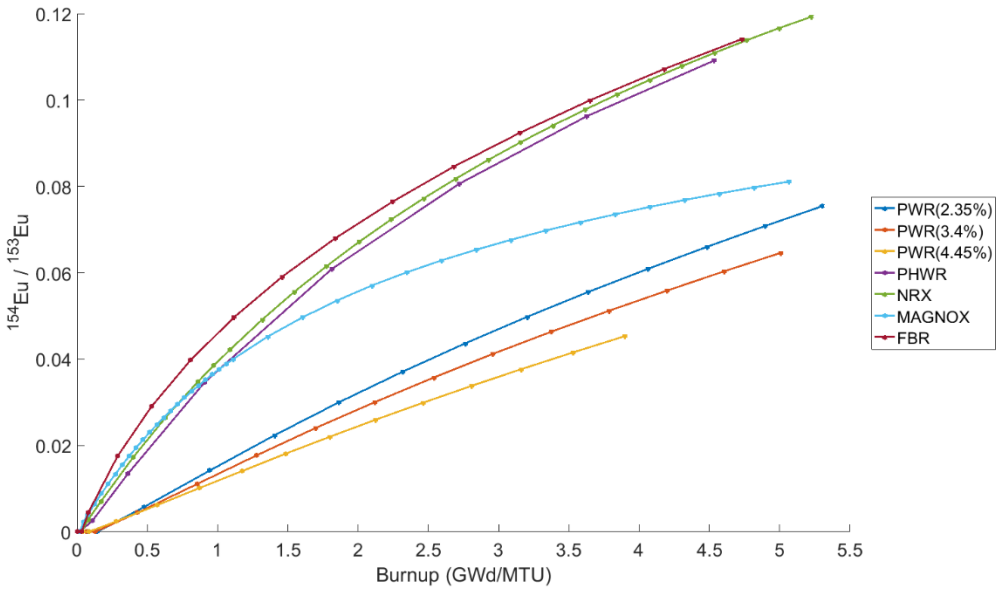

Figure 8: The ^{154}Eu/^{153}Eu ratio as a function of burnup.

The production of plutonium during irradiation begins with the radiative capture on ^{238}U which produces ^{239}Pu following two subsequent beta decays. The loss of ^{239}Pu stems from neutron absorption on ^{239}Pu which splits into fission and capture. In the case of neutron capture on ^{239}Pu the higher plutonium isotope, ^{240}Pu, is produced, and further repetitions of the neutron capture reaction lead to the production of ^{241}Pu and ^{242}Pu.

Due to a resonance in the ^{238}U cross-section for neutron capture, the production of ^{239}Pu is driven by the epi-thermal neutron flux. Given that the concentration of ^{238}U is relatively unchanged during irradiation, the rate of production of ^{239}Pu remains constant. The total neutron absorption cross-section for ^{239}Pu is significantly larger than that of ^{238}U at thermal neutron energies. As the concentration of ^{239}Pu increases so does the rate of loss of ^{239}Pu. As a result the concentration of ^{239}Pu, when plotted as a function of burnup on the X-axis, has a square root of X shape. Conversely, ^{240}Pu being produced directly from a ^{239}Pu loss mechanism has a shape resembling burnup squared. Following the further neutron capture reactions producing ^{241}Pu and ^{242}Pu, the production shapes for ^{241}Pu and ^{242}Pu resemble burnup cubed and burnup to the fourth, respectively. Dividing each plutonium isotope by ^{239}Pu, the intuitive form for the ratios of $^{240}Pu/^{239}Pu$, $^{241}Pu/^{239}Pu$, and $^{242}Pu/^{239}Pu$ are observed in Fig. 9, Fig. 10, and Fig. 11, respectively. The ratio of $^{240}Pu/^{239}Pu$ has a shape which is linear with burnup, the ratio of $^{241}Pu/^{239}Pu$ follows a burnup squared shape, and the ratio of $^{242}Pu/^{239}Pu$ follows a burnup cubed shape. The $^{242}Pu/^{239}Pu$ ratio is plotted on a semi-logarithmic scale in Fig. 12, as to highlight the grouping and separation of the reactor types.

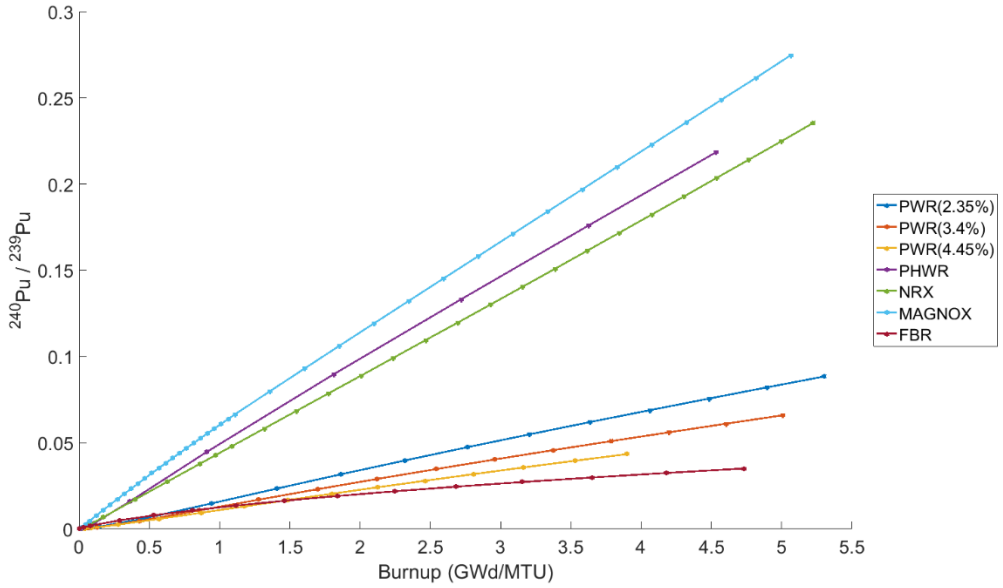

Figure 9: The $^{240}Pu/^{239}Pu$ ratio as a function of burnup.

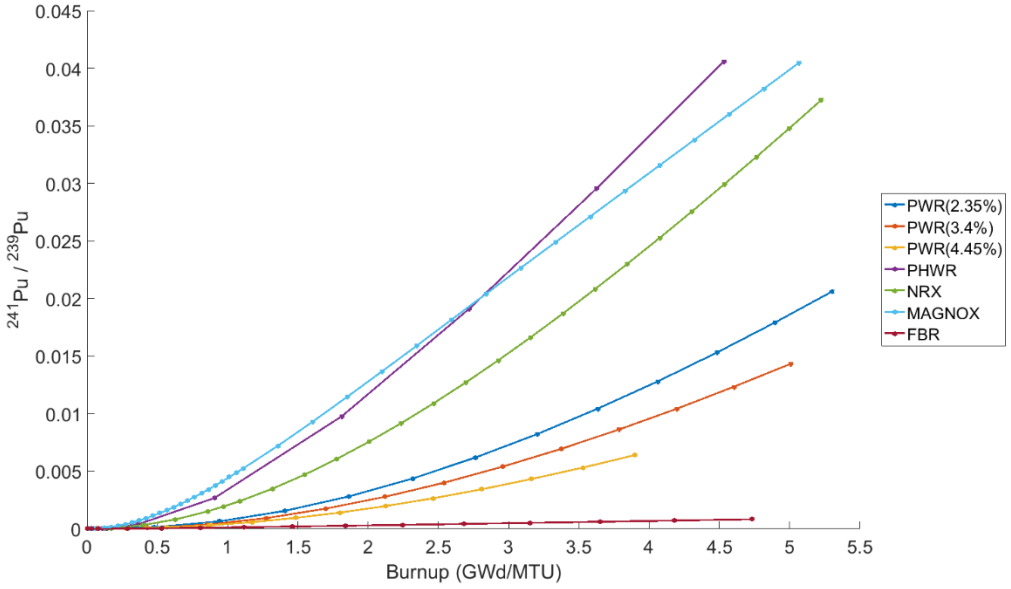

Figure 10: The $^{241}Pu/^{239}Pu$ ratio as a function of burnup.

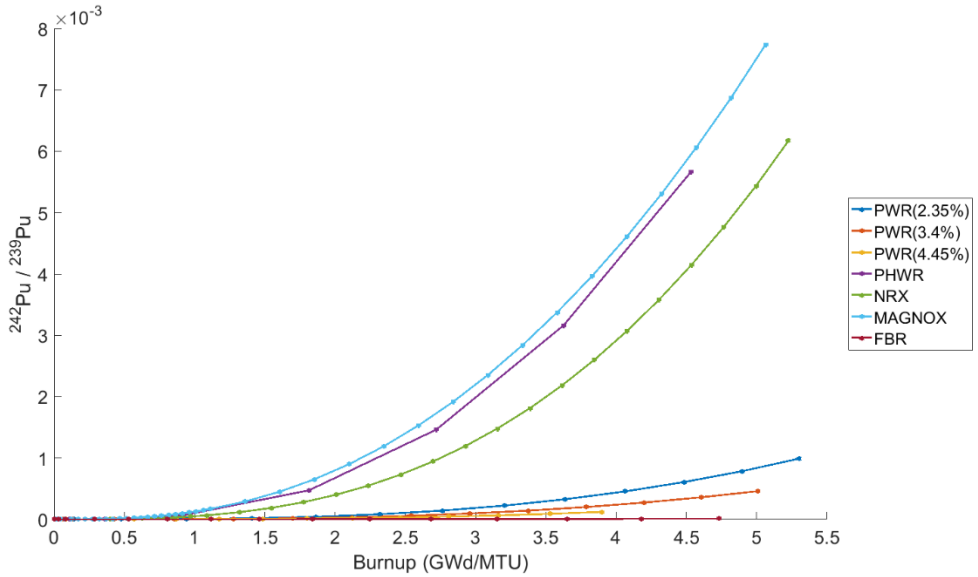

Figure 11: The $^{242}Pu/^{239}Pu$ ratio as a function of burnup.

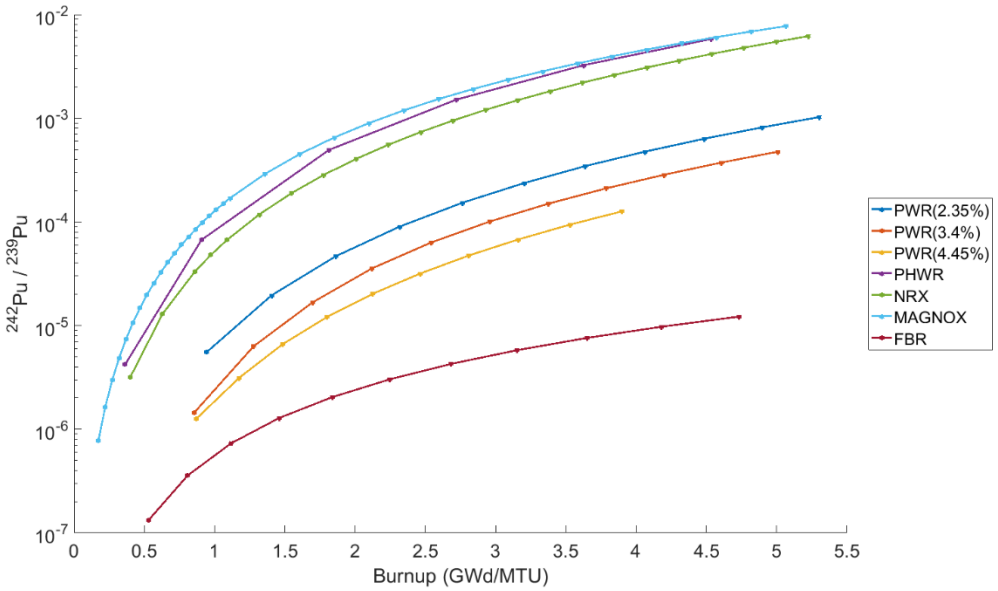

Figure 12: The $^{242}Pu/^{239}Pu$ ratio as a function of burnup plotted on a semi-logarithmic scale.

All the plutonium isotope ratios work at distinguishing amongst the reactor types. The $^{240}Pu/^{239}Pu$ ratio clearly distinguishes the natural uranium fueled thermal reactors, whereas the $^{241}Pu/^{239}Pu$ and $^{242}Pu/^{239}Pu$ ratios group and separate the natural uranium thermal reactors, enriched uranium thermal reactor, and fast reactor. For harder neutron spectra, the produced plutonium is of a better quality (greater concentration of ^{239}Pu). Given a neutron absorption, the higher incident neutron energy results in fission being more probable than radiative capture, and thus less production of the higher mass plutonium isotopes.

The step-wise depiction in this section was to illustrate the link between the intra-element isotope ratios and parameters of interest. However, the methodology developed simultaneously compares the entire set of isotope ratios. The relation between an intra-element isotope ratio and the parameters which it contributes to resolving will be case specific; however the general parameter information retained in each ratio is highlighted in Table 1.

Table 1: Parameters resolved by each intra-element isotope ratio.

Intra-Element Isotope Ratio	Parameters Resolved
$^{137}Cs/^{133}Cs$	Time Since Irradiation
$^{134}Cs/^{137}Cs$	Burnup, Time Since Irradiation
$^{135}Cs/^{137}Cs$	Reactor-Type, Time Since Irradiation
$^{136}Ba/^{138}Ba$	Burnup, Reactor Type
$^{150}Sm/^{149}Sm$	Burnup, Reactor Type
$^{152}Sm/^{149}Sm$	Burnup, Reactor Type
$^{154}Eu/^{153}Eu$	Burnup, Reactor Type, Time Since Irradiation
$^{240}Pu/^{239}Pu$	Burnup, Reactor Type
$^{241}Pu/^{239}Pu$	Burnup, Reactor Type, Time Since Irradiation
$^{242}Pu/^{239}Pu$	Burnup, Reactor Type

2.2 Maximum Likelihood Calculation as a Characterization Method

The developed reactor-type discrimination methodology utilizes a library comparison approach coupled with a maximum likelihood calculation. Computational burnup simulations were performed for each reactor model to create a reactor-dependent library of values for the ten intra-element isotope ratios of interest as a function of burnup and time since irradiation, the details of which are described in Section 3.4.

According to Bayes' theorem on random variables,[25] for an unknown parameter, θ, and observation, X, the posterior is proportional to the prior times the likelihood, as depicted in Eq. 2.

$$p(\theta|\mathrm{X}) \propto p(\theta)p(\mathrm{X}|\theta) \tag{2}$$

Applying Bayes' theorem and Eq. 2 to the reactor-type discrimination methodology, the posterior which we are calculating, shown in Eq. 3 is proportional to the probability of the reactor-type model (M), burnup (Bu), and time since irradiation (TSI) given the set of measured intra-element isotope ratio values (r_{mes}).

$$p(M, Bu, TSI|r_{mes}) \propto p(M, Bu, TSI)p(r_{mes}|M, Bu, TSI) \quad (3)$$

Here, the likelihood, $p(r_{mes}|M, Bu, TSI)$, is the probability of a measured set of isotope ratios being produced from a given reactor-type model and parameters. We assume a uniform distribution prior, $p(M, Bu, TSI)$, which means that all reactor-type models as well as values for burnup and time since irradiation are equally likely.

The maximum likelihood calculation utilizes the product of probability density values generated from reactor model simulations compared with a measured ratio value. This product is proportional to the probability that a given model with given parameters would result in observing the measured set of intra-element isotope ratio values. The largest likelihood value will be indicative of the most likely reactor model, burnup, and time since irradiation which corresponds to the set of simulated intra-element isotope ratios that most closely matches the set of measured intra-element isotope ratios. The log-likelihood is the natural logarithm of the likelihood equation. By using the log-likelihood, computational overflow errors were avoided in the calculation. The likelihood, *L*,[26] and log-likelihood, *Log L*, of reactor model, *M*, with burnup, *Bu*, and time since irradiation, *TSI*, matching the measured set of intra-element ratios, r_{mes}, can be written as:

$$L(M, Bu, TSI|r_{mes}) \propto L(r_{mes}|M) = \prod_{j=1}^{n} \frac{1}{\sigma_{j,sim}\sqrt{2\pi}} exp\left\{-\frac{(r_{j,mes}-r_{j,sim})^2}{2\sigma_{j,sim}^2}\right\} \quad (4)$$

$$Log\ L(M, Bu, TSI|r_{mes}) = \sum_{j=1}^{n} \left[log\left(\frac{1}{\sigma_{j,sim}\sqrt{2\pi}}\right) - \frac{(r_{j,mes}-r_{j,sim})^2}{2\sigma_{j,sim}^2}\right] \quad (5)$$

Where:

$r_{j,mes}$ = j^{th} intra-element isotope ratio (for example $^{137}Cs/^{133}Cs$) in a set of *n* measured intra-element ratios

$r_{j,sim}$ = j^{th} intra-element isotope ratio in a set of *n* simulated intra-element ratios from model, *M*, within the reactor library

$\sigma_{j,sim}$ = the simulation uncertainty associated with the j^{th} intra-element ratio value from the set, r_{sim}

The logarithm is a strictly increasing function thus, the set of simulated intra-element isotope ratio values which maximizes the likelihood is also the same set of simulated values which maximizes the log-likelihood.

By using the propagation of uncertainty, the variance in the log-likelihood in Eq. 5 can be calculated. With the log-likelihood being a function of two variables, Log-$L(r_{mes},r_{sim})$, the variance can be expanded as:

$$\sigma_{Log\ L}^2 = \left(\frac{\partial\ Log\ L}{\partial\ r_{mes}}\right)^2 \times \sigma_{j,mes}^2 + \left(\frac{\partial\ Log\ L}{\partial\ r_{sim}}\right)^2 \times \sigma_{j,sim}^2 \quad (6)$$

Taking the partial derivative of the log-likelihood, Eq. 5, with respect to r_{mes} yields:

$$\frac{\partial}{\partial\ r_{mes}}\left(\sum_{j=1}^{n}\left[log\left(\frac{1}{\sigma_{j,sim}\sqrt{2\pi}}\right) - \frac{(r_{j,mes}-r_{j,sim})^2}{2\sigma_{j,sim}^2}\right]\right) = \sum_{j=1}^{n} -\frac{(r_{j,mes}-r_{j,sim})}{\sigma_{j,sim}^2} \quad (7)$$

Taking the partial derivative of the log-likelihood, Eq. 5, with respect to r_{sim} yields:

$$\frac{\partial}{\partial\, r_{sim}}\left(\sum_{j=1}^{n}\left[log\left(\frac{1}{\sigma_{j,sim}\sqrt{2\pi}}\right)-\frac{\left(r_{j,mes}-r_{j,sim}\right)^2}{2\sigma_{j,sim}^2}\right]\right)=\sum_{j=1}^{n}\frac{\left(r_{j,mes}-r_{j,sim}\right)}{\sigma_{j,sim}^2} \quad (8)$$

Thus, the variance in the log-likelihood can be written as:

$$\sigma_{Log\,L}^2=\sum_{j=1}^{n}\left(\frac{\left(r_{j,mes}-r_{j,sim}\right)}{\sigma_{j,sim}^2}\right)^2\times\left(\sigma_{j,mes}^2+\sigma_{j,sim}^2\right) \quad (9)$$

where, $\sigma_{j,mes}$ is the measurement uncertainty associated with the j^{th} intra-element ratio value from the set, r_{mes}. The likelihood value will be used for visualization, whereas the log-likelihood value and uncertainty in the log-likelihood will be used to identify the most likely reactor model and associated parameters that could have produced the measured material.

Figure 13 depicts a visualization of the developed reactor-dependent intra-element isotope ratio library. For each reactor model, a 500 burnup step x 5000 time since irradiation step matrix is created, both of which are discussed in Section 3.4. At each point on the matrix, the ten simulated intra-element isotope ratios corresponding to the burnup and time since irradiation are compared to the set of ten measured ratios using Eq. 5. The result is a log-likelihood value at each point on the reactor-dependent matrix. The location of the maximum log-likelihood value corresponds with the predicted values of burnup and time since irradiation. The largest log-likelihood value among the reactor types will indicate the most likely reactor to be the source of the measured material.

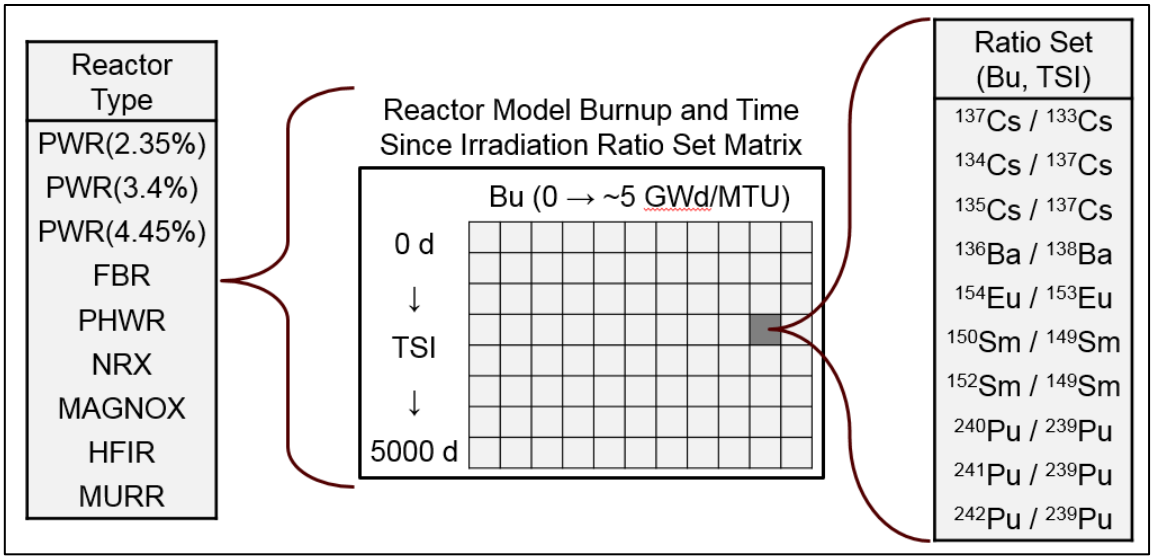

Figure 13: Visualization of the reactor-dependent intra-element isotope ratio library.

3. MCNP MODELING AND REACTOR LIBRARY*

3.1 Monte Carlo N-Particle (MCNP) Transport Code

Each reactor model contained in the reactor library was developed and simulated using one of two versions of the Monte Carlo radiation transport codes, MCNPX Version 2.7[27] and MCNP6[28]. MCNP is a general-purpose, continuous-energy, generalized-geometry Monte Carlo radiation-transport code designed to track particle interactions.[28] The user creates an input file containing information regarding geometry specifications, material descriptions, selection of interaction cross-section evaluations, location and characteristics of the radiation particle source, type of output information desired, and any variance reduction techniques if applicable.[28]

The Monte Carlo method is a numerical analysis technique which uses random sampling procedures to construct the solution of a physical problem. A stochastic model estimates the statistical numerical answers to the problem by sampling from appropriate probability distributions, in this case the Boltzmann Transport Equation.[29] The Monte Carlo method in MCNP simulates the process of nuclear particle interactions with matter by sampling, via random numbers, probability distributions calculated from transport data.[30]

---

* Reprinted with permission from "Nuclear Forensics Methodology for Reactor-Type Attribution of Chemically Separated Plutonium" by J.M. Osborn *et al.*, 2017. *Nucl. Tech.*, 201, 1-10, Copyright 2017 by American Nuclear Society.

* Reprinted with permission from "Computational and experimental forensics characterization of weapons-grade plutonium produced in a thermal neutron environment" by J.M. Osborn *et al.*, 2018. *Nucl. Eng Technol.*, 50, 820-828, Copyright 2018 by Korean Nuclear Society.

The MCNP code must have an abundant supply of random numbers uniformly distributed between 0 and 1. Each particle is followed from birth to the particle's death or escape from the system, with random sampling of probability distributions contained in the radiation transport equation to determine the outcome at each step of the particle's life.[29] Events in the life of a particle may include the distance between collisions, collision nuclide selection, and nuclear reaction selection. Probabilities at each event are calculated based on physics, transport data and the materials involved. A random number is selected at an event and applied to the probability distribution to determine the outcome of the event. This process is repeated along the particle's life with a particle's death coming from absorption or leakage from the system. As a large number of particle life histories are tracked, the average particle behavior better simulates the physical process.[30]

The MCNP code indirectly solves the integral form of the Boltzmann Transport Equation by simulating individual particle life histories and averaging the behavior of a large number of particles using the Monte Carlo numerical method. Monte Carlo is well suited for solving complicated three-dimensional, time-dependent problems,[30] making MCNP suitable for use in this research work.

3.2 CINDER90 Depletion

During the operation of a nuclear reactor, the fuel materials will undergo changes to the isotopic composition, due to neutron interactions. The neutron reaction cross-sections with the fuel isotopes along with the neutron flux in the reactor will dictate the rate of change of the isotopic composition. The temporal change in isotopic

compositions further alter the subsequent reaction rates. As a result, it is essential to capture the temporal isotopic concentrations of the materials in the reactor in order to accurately simulate reactor operation through fuel burnup.[31]

Both versions of the MCNP code used in this study calculate fuel burnup via the integrated depletion/burnup module, CINDER-90.[32] Fuel depletion/burnup calculations are a linked process involving neutron flux and reaction rate calculations in MCNP and nuclide depletion calculations in CINDER90. MCNP performs a steady-state calculation to determine a 63-group neutron flux, which is energy-integrated with nuclide transport cross-sections resulting in reaction rates. CINDER90 takes the MCNP-generated data, neutron fluxes and reaction rates, and performs the depletion calculation to obtain new isotopic compositions for the next burnup time step. This process is repeated for each burnup time step, specified by the user, until the entire burnup simulation is completed.[32] Upon completion of the burnup calculation, MCNP will provide an output containing the neutronics and burnup data for the spent fuel, including criticality, average neutrons released per fission, average energy released per fission, level of burnup, and isotopics of the spent fuel.

Solving for the temporal change in an isotope composition requires accounting for the nuclear reactions which cause production or loss of the nuclide, and may be described by the Bateman equations.[31] A simplified form of the Bateman equations for a specified isotope is:[31,32]

$$\frac{dN_i}{dt} = -N_i(t)\beta_i + \overline{Y}_i + \sum N_k(t)\gamma_{k\rightarrow i} \quad (10)$$

Where:

$\frac{dN_i}{dt}$ = time-dependent change in isotope i

$N_i(t)$ = the time-dependent atom density of isotope i

β_i = the total transmutation probability of isotope i

$\overline{Y}_i$ = production of isotope i via an external source

$\gamma_{k \to i}$ = the probability of an isotope k transmuting, by decay or absorption, into isotope i

Equation 10 is nonlinear because the transmutation probabilities rely on the time-integrated flux, which is also reliant upon the time-dependent isotope compositions.[32] To make the equation linear, the assumption must be made that the transmutation probabilities, and thus neutron flux, remain constant over the burnup time step. This assumption requires attention when selecting the number and duration of burnup time steps. A larger number of steps will lead to a larger computational run time. However, a time step with too long of a duration will not be appropriate for assuming the neutron flux and transmutation probabilities are constant for the time step. In CINDER90, the set of coupled differential equations is reduced to a set of linear differential equations using the Markov Linear Chain method.[31] Linear chains are created for each isotope transmutation path and generate Eq. 11, where γ_{i-1} is the transmutation probability of forming isotope N_i.[32]

$$\frac{dN_i}{dt} = -N_i(t)\beta_i + \overline{Y}_i + N_{i-1}(t)\gamma_{i-1} \tag{11}$$

The solution to each linear chain determines a partial isotope composition, which is then summed to obtain the total isotope inventory. Due to the use of these linear chains, the isotopic inventory is only coupled to preceding elements in the sequence, where the parameters are assumed known.[31] The general solution to such a linear sequence is as follows in Eq. 12.[31,32]

$$N_n(t) = \prod_{k=1}^{n-1}\gamma_k \left\{\overline{Y}_m \left[\frac{1}{\prod_{l=1}^{n}\beta_l} - \sum_{j=1}^{n}\frac{e^{-\beta_j t}}{\prod_{i=1,\neq j}^{n}(\beta_i-\beta_j)}\right] + N_1^0 \sum_{j=1}^{n}\frac{e^{-\beta_j t}}{\prod_{i=1,\neq j}^{n}(\beta_i-\beta_j)}\right\} \quad (12)$$

3.3 Predicting Stochastic Error in Isotope Concentrations

As mentioned in the previous section, fuel burnup/depletion calculations are a coupled process between MCNP and CINDER90. MCNP calculates steady-state neutron flux and reaction rates, and provides CINDER90 with the neutron reaction rate data necessary to perform burnup/depletion calculations and predict isotopic concentrations for the next time step.

The MCNP portion of each burn step calculates isotope-specific reaction rates as well as the error associated with each reaction rate. However, the reaction rate errors are not used by CINDER-90 when calculating burnup and isotopic concentrations, and thus the errors in such predictions are not propagated through MCNP burnup simulations. An error in the simulated prediction of each isotopic concentration must be assumed. For the maximum likelihood analysis presented in Section 9, a 10% simulation error was assumed for the concentration of each isotope. Propagated together, this leads to an error of approximately 14% as the uncertainty for each simulated ratio value.

While an error in the simulated isotopic concentrations was assumed for the maximum likelihood analysis in Section 9, we desired to outline a framework for how

the user may determine the stochastic error in the simulated isotopic concentrations. This is made possible by using results of the isotopic reaction rates and reaction rate errors obtained at each step of a burnup simulation. With a knowledge of all the important reactions which contribute to the production and loss of a specific isotope, the significant reaction rates and errors can be manually propagated together and through each time step. Here we have used the reaction rate errors to estimate the stochastic error in the predicted burnup, which is synonymous with the predicted ^{137}Cs concentration, and the total plutonium mass from the simulations of the experimental irradiations at HFIR and MURR.

^{137}Cs is a direct fission product since the precursors to ^{137}Cs are short lived and have negligible capture cross sections. The contribution from the radiative capture on ^{136}Cs is negligible, thus the cumulative fission yield can be considered the only production mechanism of ^{137}Cs. The cross-section for any loss of ^{137}Cs is negligible with the only loss mechanism for ^{137}Cs being decay ($t_{1/2}$ = 30.08 y). The time derivative and time integral expressions for the production of ^{137}Cs during irradiation are as follows:

$$\frac{d}{dt_i}\left(^{137}Cs(t_i)\right) = N_{fuel} * V_{fuel} * \sigma_{fission} * \varphi * Y_{137} - {}^{137}Cs(t_i) * \lambda_{137Cs} \quad (13)$$

$$^{137}Cs(t_i) = N_{fuel} * V_{fuel} * \sigma_{fission} * \varphi * Y_{137}\left(1 - e^{-\lambda_{137Cs} * t_i}\right) \quad (14)$$

Where:

N_{fuel} = the atom density of the fuel (atoms/cm^3)

V_{fuel} = the volume of the fuel (cm^3)

$\sigma_{fission}$ = the microscopic fission cross-section (cm^2/atom)

φ = the neutron flux (n/cm^2-s)

Y_{137} = the cumulative fission yield fraction for ^{137}Cs

λ_{137Cs} = is the radioactive decay constant for ^{137}Cs (s^{-1})

^{137}Cs will decay following the completion of irradiation. Ignoring the loss during irradiation due to decay, the concentration of ^{137}Cs depends on total fissions and the fission yield. If we assume the fission yield for ^{137}Cs is similar among all fissioning isotopes then the ^{137}Cs production and error is proportional to the total fission rate and error.

At each burn step, the total step fissions as well as the step fission error were calculated by summing the fission reaction rates for all fissioning isotopes, propagating the isotope fission reaction rate errors, and multiplying each by the step duration.

$$Step\ Fissions = \left[\sum_i (n, fission)_i\right] \times Duration \tag{15}$$

$$Step\ Fission\ Error = \sqrt{\sum_i \{(n, fission)_i \times RE_i\}^2} \times Duration \tag{16}$$

Where:

$(n, fission)_i$ = the fission rate for fissioning isotope, i (fissions/s)

$Duration$ = the step duration (s)

RE_i = the fission rate relative error for fissioning isotope, i

Next, the total fissions and total fission error for each burn step was propagated through the entire burnup simulation, resulting in a calculated stochastic relative error in the total fissions from the MCNP simulation. This stochastic relative error in the total

fissions will equally be the stochastic relative error in the predicted ^{137}Cs concentration and the predicted burnup.

$$Total\ Fissions = \sum_{\substack{Number \\ of\ Steps}} (Step\ Fissions) \tag{17}$$

$$Total\ Fission\ Error = \sqrt{\sum_{\substack{Number \\ of\ Steps}} (Step\ Fission\ Error)^2} \tag{18}$$

For the predicted mass of plutonium, a similar process was followed by propagating the reaction rates and reaction rate errors for the neutron capture on ^{238}U and the fission of ^{239}Pu, the primary production and loss mechanisms for plutonium, respectively. All other reaction rates leading to the production or loss of plutonium are several order of magnitudes lower, and insignificant in calculating the mass of plutonium production at a low level of burnup. The calculated stochastic errors are present due to the random nature of the Monte Carlo calculation, and do not include systematic errors within the model and simulation. The stochastic error refers only to the precision of the calculation itself and not the accuracy of the results compared to the true physical value. To assess the accuracy requires detailed information regarding systematic uncertainties in cross-section data, yield data, modeling, and approximations.[30] The process of propagating errors from multiple time steps verifies the assumption that a larger number of time steps within a burnup calculation yields a stochastically more precise result.

3.4 Reactor Library

Reactor operation of each model was simulated to a burnup of approximately 5 GWd/MTU, expanded to 500 burnup intervals by linear interpolation, and used to generate the intra-element isotope ratio values, discussed in Section 2.1, in the irradiated

fuel as a function of burnup. For isotopes having short-lived precursors, at each burn step the short-lived precursors were summed with the isotope of interest. This allows the ratio values, as a function of burnup, to be representative of a measured value at a later measurement date. A set of decay equations calculates the intra-element isotope ratios from each burnup interval as a function of time since irradiation ended ranging from 0 to 5000 days (1-day intervals). Consequently, for each reactor model, the reactor-dependent library consists of a 500 burnup step x 5000 time since irradiation step matrix containing values of the set of intra-element isotope ratios.

The reactor library consists of seven power reactor-type models. These common power reactors all have an ability to produce weapons-useable plutonium by discharging irradiated fuel at a burnup less than 5 GWd/MTU. FBRs can produce weapons-useable plutonium in the depleted uranium dioxide (DUO_2) blanket material, the region which surrounds the core. Under normal reactor operation, the blanket assemblies are designed to be discharged at a low fuel burnup less than 2.0 GWd/MTU.[33] Previous work has estimated that about 140 kg of weapons-useable plutonium will be produced in the blankets of an FBR each year.[34,35] Therefore, any country operating an FBR will be generating significant quantities of weapons-useable plutonium in the blanket material. The core characteristics for the FBR modeled here are readily available via open literature.[33,34] FBR burnup simulations were performed for the DUO_2 radial blanket where plutonium is produced. Although this level of burnup is impractical for the blanket region of an FBR; the FBR model simulated the fuel burnup of the blanket material to approximately 5 GWd/MTU for comparison with the other reactors.

Figure 14 provides an FBR core map highlighting the inner and outer "driver" cores, as well as the DUO_2 fueled radial blanket. Figure 15 illustrates an MCNP rendering of an FBR radial blanket assembly.

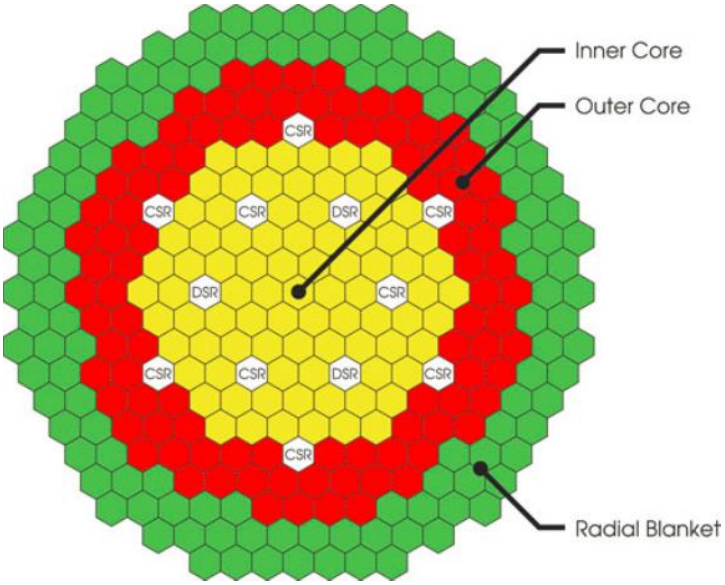

Figure 14: FBR core map.

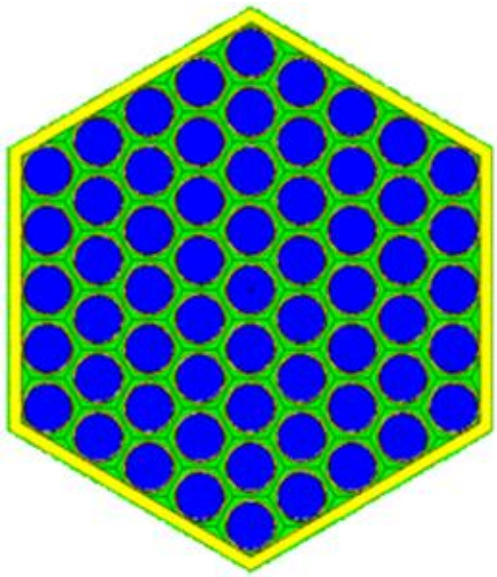

Figure 15: A radial cross section of an FBR radial blanket assembly in MCNP.

Natural uranium fueled reactors are a proliferation concern due to their proficiency at producing plutonium. Natural uranium fuel has a lower reactivity worth than enriched uranium, leading to the need for natural uranium reactors to be refueled more frequently and at a lower burnup. As a result the design of most natural uranium reactors incorporates an online refueling capability, which has an inherent susceptibility to discharging fuel at lower than normal burnup for diversion of weapons-usable plutonium. A design hurdle among natural uranium fueled reactors is that normal (light) water cannot be used for the neutron moderator and still maintain the neutron economy necessary for sustained criticality, due to neutron absorption losses in light water. Two alternative moderator materials typically used in natural uranium reactors are heavy water (deuterium oxide) or graphite. The 40-MWth Canadian NRX reactor and the 182-MWth British Magnox reactor were the first natural uranium fueled heavy-water

moderated and graphite moderated reactor designs, respectively. Both of these were originally designed for the purpose of producing plutonium for weapons programs.[36,37]

Several states have used heavy-water reactors to expand their plutonium production capabilities.[38] Israel's Dimona reactor, Pakistan's Khushab reactors, and India's CIRUS and DHRUVA reactors are all based off the NRX reactor design and all operated outside of international safeguards.[38,39,40,41,42] Each of these NRX-type reactors is predicted to have the ability to produce 7 kg or more of plutonium per year.[38] The NRX reactor modeled for the current study was Iran's IR-40.[38,43] An MCNP rendering of the IR-40 fuel assembly is shown in Fig. 16. The 40 MWth NRX-type IR-40 reactor at Arak was anticipated to be completed and operating by 2014.[44] As part of the process leading to the conclusion of the Joint Comprehensive Plan of Action in 2015, Iran halted construction on the IR-40 in 2013.[45]

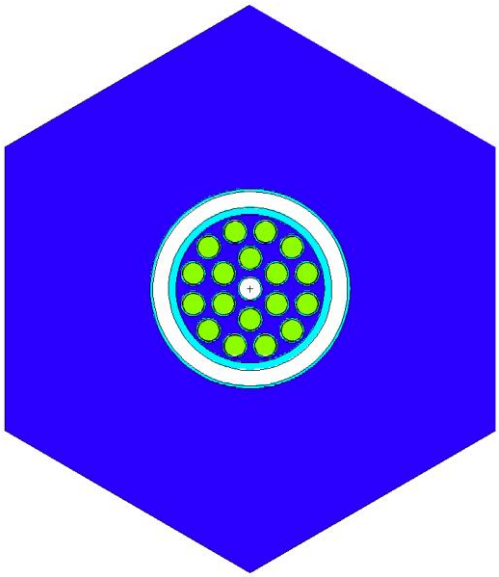

Figure 16: A radial cross section of a NRX fuel assembly in MCNP.

In 1986 North Korea completed development of a smaller version of the British Magnox reactor at Calder Hall based on declassified design information.[24] The Yongbyon reactor has a thermal power output of 25 MWth and utilizes natural uranium fuel, graphite for moderation, and carbon dioxide for cooling. The Yongbyon reactor has been the sole source of plutonium for the North Korean weapons program. Under normal operation it is estimated that the Yonbyon Magnox-type reactor can produce approximately 6 kg of plutonium per year.[24] The Magnox reactor modeled in this study was the Yongbyon reactor, and the MCNP core map displayed in Fig. 17.[37,46]

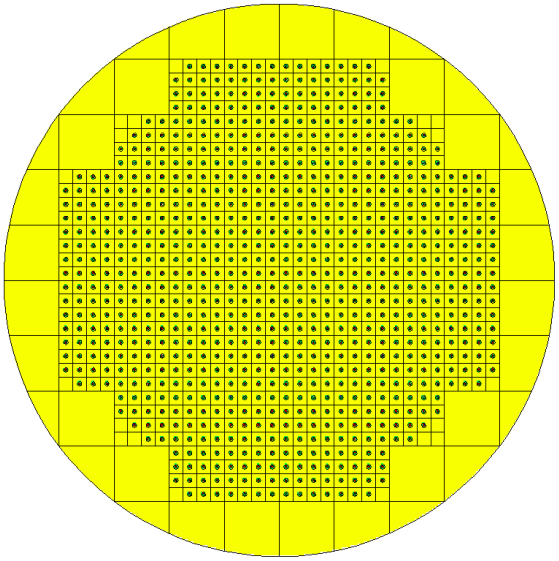

Figure 17: Magnox core map in MCNP.

The majority of India's operating power reactors are PHWRs. For some of these PHWRs which have not been placed under IAEA safeguards, they could serve a dual purpose of energy production as well as non-civilian plutonium production. The PHWR

has a primary purpose of electricity generation and typically discharges fuel at a burnup of 7.5 GWd/MTU. However, similar to the other natural uranium fueled reactors, the PHWR has an online refueling capability which leads to a susceptibility for fuel to be discharged at a low burnup to obtain weapons-useable plutonium. The specific PHWR-type reactor modeled in the current study was an Indian 220-MWe PHWR.[47] A cross section view of the PHWR fuel assembly in MCNP is illustrated in Fig. 18.

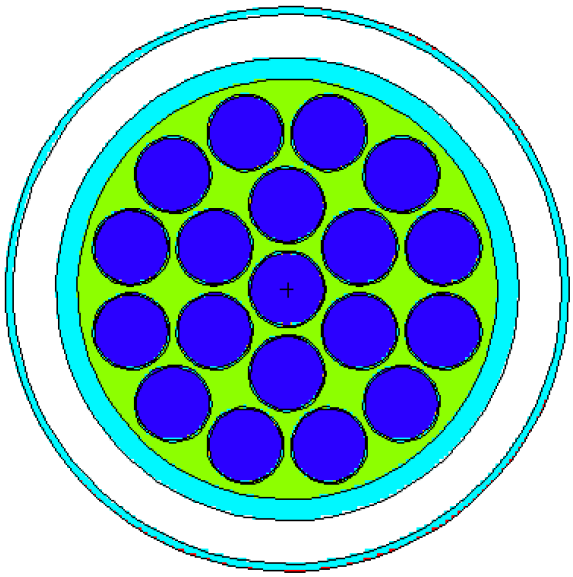

Figure 18: A radial cross section of a PHWR fuel assembly in MCNP.

PWR fuel typically reach a higher average burnup of 45 GWd/MTU. Unlike PHWRs, PWRs cannot be refueled during reactor operation. The theorized situation in which a PWR would result in weapons-useable plutonium production would be an unplanned reactor shutdown during which low-burnup fuel assemblies may be diverted. The AP1000[48] was modeled to represent the PWR, and the cross section view of a PWR

fuel assembly in MCNP is illustrated in Fig. 19. PWR burnup simulations were performed for fuel assemblies at enrichments of 2.35 wt%, 3.4 wt%, and 4.45 wt% ^{235}U.

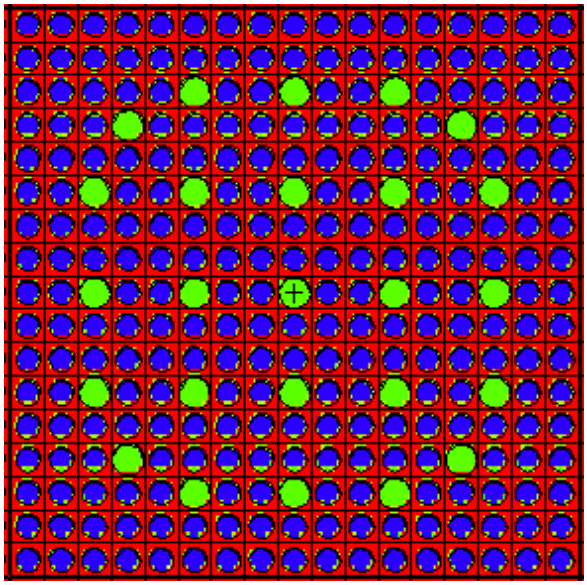

Figure 19: A radial cross section of a PWR fuel assembly in MCNP.

The three-dimensional reactor core models of these power reactors were created based on publicly available information from literature. The effects of refueling and the presence of control rods are not included in these simulations. This research focuses on the core averaged fission product and plutonium concentrations as a function of burnup. While axial and radial special discrepancies within a reactor core may exist for isotopic concentrations as a function of burnup, it is assumed these special differences will be less significant than the differences between the different reactor types.

In addition to these power reactor-types, the reactor library includes two simulations of the experimental irradiations performed at HFIR and MURR for use in

the validation study of the nuclear forensics methodology. The HFIR core was developed by ORNL for reactor cycle 400[49] and provided as part of support for the experimental irradiation. The model was modified to include the DUO_2 fuel discs and gadolinium capsule in the irradiation location. The HFIR model was used to produce best estimate values for the material isotopics at the end of the experimental irradiation. Additionally, the HFIR model simulation was extended past the known irradiation to a burnup of approximately 5 GWd/MTU for consistency within the reactor library. Details of the experimental irradiation at HFIR can be found in Section 4 as well as Swinney *et al*.[13,14] The MURR core was developed based on reactor characteristics found in the 2006 MURR Safety Analysis Report (SAR).[50] Information on the irradiation location and a detailed irradiation history was provided from MURR staff. The MURR model was used to produce best estimate values for the material isotopics at the end of the experimental irradiation. Additionally, the MURR model simulation was extended past the known irradiation to a burnup of approximately 5 GWd/MTU for consistency within the reactor library. Details of the experimental irradiation at MURR are discussed in Section 5. The HFIR and MURR models contained in the reactor library are not indicative of the HFIR and MURR reactor cores, but rather the sample material irradiation which took place within each reactor facility. Table 2 contains some key parameters of the reactor cores modeled.

Table 2: Reactor library model characteristics.[33,37,38,43,46,47,48,49,50]

Reactor Model	Thermal Power (MWth)	Fuel Type (at.% ^{235}U)	Moderator	Coolant
PWR (2.35%) [a]	3400	UO_2 (2.35)	Light Water	Light Water
PWR (3.4%) [a]	3400	UO_2 (3.4)	Light Water	Light Water
PWR (4.45%) [a]	3400	UO_2 (4.45)	Light Water	Light Water
FBR	1250	UO_2 (0.25) [b]	-	Liquid Sodium
PHWR	756	UO_2 (0.72)	Heavy Water	Heavy Water
NRX	40	UO_2 (0.72)	Heavy Water	Heavy Water
Magnox	25	U metal w/ 0.5% Al (0.72)	Graphite	Carbon Dioxide
HFIR	85	UO_2 (0.25) [c]	Light Water	Light Water
MURR	10	UO_2 (0.72) [d]	Light Water, Beryllium, Graphite	Light Water

[a] The PWR model has fuel assemblies at three different enrichments (2.35%, 3.4%, and 4.45% ^{235}U enrichment).

[b] The FBR has a MOX core and depleted UO_2 blanket region. The material analyzed here is from the FBR radial blanket region.

[c] The HFIR model is not indicative of the HEU-fueled HFIR core. Rather, the HFIR model is a simulation of the experimental irradiation at HFIR plus an extension to a burnup of approximately 5 GWd/MTU.

[d] The MURR model is not indicative of the HEU-fueled MURR core. Rather, the MURR model is a simulation of the experimental irradiation at MURR plus an extension to a burnup of approximately 5 GWd/MTU.

4. MCNP SIMULATION OF THE EXPERIMENTAL DEPLETED UO_2 IRRADIATION AT HFIR

The first experimental irradiation was designed to represent weapons-usable plutonium produced in the blanket of a fast breeder reactor. The High Flux Isotope Reactor (HFIR) at Oak Ridge National Laboratory (ORNL) was chosen to perform the depleted UO_2 fuel sample irradiation. As with the other research reactors available to us for sample irradiations, the HIFR is a thermal neutron reactor. In order to replicate the fast neutron spectrum of an FBR blanket, the depleted UO_2 fuel samples were irradiated within a gadolinium capsule which would absorb the thermal component of the neutron flux. The large neutron flux magnitude of HFIR meant that, while removing the thermal component of the neutron flux, the flux magnitude was large enough to reach the desired burnup of approximately 1 GWd/MTU in a timely manner. A recent dissertation study conducted by Mathew W. Swinney[14] at Texas A&M University detailed the experimental irradiation at HFIR, MCNP simulation of the experimental irradiation at HFIR, and an experimental characterization of the irradiated fuel material. Information pertinent to the HFIR irradiated test material in addition to further developments of the MCNP simulation are contained here.

4.1 Fuel Sample Description

The six fuel samples were depleted UO_2 discs fabricated by ORNL using uranium (0.2562 wt% ^{235}U) powder supplied by AREVA. Table 3 contains the actual disc characterization reported by ORNL. Six identical discs were modeled in the MCNP

simulation. The modeled disc had dimensions of 0.02 cm in thickness and 0.153 cm in radius, with a density of 10.5 g/cm^3 and mass of 15.4 mg.

Table 3: Depleted UO_2 disc characterization.

Disc	Mass (g)	Radius (cm)	Thickness (cm)	Density (g/cc)
01A	0.0135	0.140	0.0223	9.90
01B	0.0139	0.140	0.0217	10.33
03A	0.0144	0.141	0.0228	10.11
05A	0.0157	0.138	0.0260	10.17
05B	0.0132	0.138	0.0209	10.63
06A	0.0130	0.138	0.0205	10.60

4.2 Description of the High Flux Isotope Reactor (HFIR)

The HFIR is a flux-trap type, highly-enriched uranium (HEU) fueled, pressurized light water moderated and cooled reactor surrounded by a beryllium reflector.[49] The annular reactor core consists of two concentric fuel elements separated by water, and surrounding the flux-trap irradiation locations. The central flux-trap provides a large thermal neutron flux (2.6×10^{15} neutrons/cm^2-s) for material irradiations. Table 4 shows the reactor characteristics of the HFIR core obtained from a report published by ORNL for HFIR cycle 400.[49]

Table 4: Summary of HFIR reactor parameters.[49]

Parameter	Value
Reactor Power (MWth)	85
Reactor Core Geometry	Annular
Fuel Material	U_3O_8-aluminum
Fuel Enrichment	93.1% ^{235}U
Total ^{235}U Loading (kg)	9.43
Fuel Assembly Cladding	Aluminum
Inner Fuel Element Number of Fuel Plates	171
Outer Fuel Element Number of Fuel Plates	369
Fuel Plate Thickness (mm)	1.27
Coolant	Light Water
Control Elements	Europium, Tantalum
Reflector Material	Beryllium
Reflector Thickness (cm)	30

4.3 Description of the Irradiation at HFIR

The six discs were surrounded by gadolinium spacers, all of which were housed in an aluminum irradiation capsule. The gadolinium spacers were utilized to absorb the thermal component of the HFIR neutron flux. Within the HFIR flux-trap the irradiation tool place in the C-5 position in vertical location 7, which occupies a position approximately 15.6 to 22.1 cm above reactor center. The irradiation occurred during HFIR cycles 446 and 447, with a 94 day shutdown for refueling in between. The total irradiation time was approximately 50.25 effective full-power days (EFPDs) at the rated power of 85 MWth, and ending on June 1, 2013. The specific fuel sample irradiation history is contained in Table 5.

Table 5: Fuel sample irradiation history during the experimental irradiation at HFIR.

Irradiation Start Date & Time	Irradiation End Date & Time	Days Irradiated
1/8/2013 8:22	5/7/2013 6:17	24.98
2/2/2013 7:49	6/1/2013 12:51	25.27

4.4 HFIR Model and Burnup Simulation

The MCNP model of the HFIR core used was developed by ORNL for reactor cycle 400.[49] The model was modified by Swinney to include the six depleted UO_2 samples, gadolinium spacers, and irradiation capsule. The core fuel was not depleted during the burnup simulation. Thus the depleted UO_2 samples and gadolinium spacers of the irradiation capsule were the only materials in which burnup was tracked using the CINDER-90 module of MCNP.

For the HFIR model contained in the reactor library, the original burnup simulation performed by Swinney was used, in which two 25 day full power cycles with a 94 day shutdown in between were simulated over nine burnup time steps.[14] The simulation was further extended by three 0.5 day full power steps in order to extend the simulated burnup past 5 GWd/MTU. The simulation was performed with 10^5 particles per cycle and 10^4 cycles for every burnup time step.

The material characterization done by Swinney concluded that the fuel samples were irradiated to a burnup of 4.36 ± 0.28 GWd/MTU, significantly higher than the intended burnup of 1 GWd/MTU. The discrepancy was attributed to human error. The simulation used by ORNL to determine that approximately 50 days of irradiation would be needed to reach the intended burnup was at a different vertical location than where

the actual fuel samples were placed during irradiation. During the actual irradiation, the samples were approximately 2.45 cm closer to the core mid-plane than in the predictive simulation. This difference resulted in the samples being exposed to a significantly larger flux than predicted.[14] Further investigations carried out as part of this study and presented in Section 9.2 indicate that after approximately 1 GWd/MTU of burnup, depletion of the Gd irradiation capsule resulted in the DUO_2 discs being irradiated within a thermal neutron spectrum for the remainder of the irradiation instead of the intended fast neutron spectrum. The increasingly large thermal neutron spectrum contributed significantly to the unexpectedly high burnup.

5. MCNP SIMULATION OF THE EXPERIMENTAL NATURAL UO_2 IRRADIATION AT MURR*

The second experimental irradiation was designed to represent weapons-usable plutonium produced in a natural uranium fueled thermal reactor. The University of Missouri Research Reactor (MURR) was chosen to perform the natural UO_2 fuel sample irradiation. The MURR facility is designed for material irradiations, and the thermal neutron flux magnitude in the irradiation locations are large enough to reach the desired burnup of approximately 1 GWd/MTU in a timely manner.

5.1 Fuel Sample Description

The fuel samples were natural UO_2 discs fabricated by Oak Ridge National Laboratory, Oak Ridge, Tennessee for Texas A&M University. Three discs were sent to MURR for the irradiation campaign. Table 6 shows the actual disc characterization reported by ORNL, and the average disc characteristics used for MCNP simulations. From the ORNL report, there was a discrepancy between the reported masses and the reported disc dimensions and densities. The reported mass was assumed to be the most reliable characteristic, and the average disc was calculated conserving the total mass. The three simulated discs were 0.224 mm in thickness and 3.0 mm in diameter, with a density of 10.4 g/cm^3 and a mass of 16.46 mg.

* Reprinted with permission from "Computational and experimental forensics characterization of weapons-grade plutonium produced in a thermal neutron environment" by J.M. Osborn *et al.*, 2018. *Nucl. Eng Technol.*, 50, 820-828, Copyright 2018 by Korean Nuclear Society.

Table 6: Natural UO_2 disc characterization.

Disc	Mass (g)	Radius (cm)	Thickness (cm)	Density (g/cc)
14-B	0.0166	0.15	0.023	10.46
15-A	0.0161	0.15	0.024	10.46
15-B	0.0167	0.15	0.024	10.46
Simulated	0.0165	0.15	0.022	10.4

5.2 Description of the University of Missouri Research Reactor (MURR)

The MURR is a highly-enriched uranium (HEU) fueled, light water moderated and cooled reactor surrounded by beryllium and graphite reflectors. The annular reactor core consists of eight sectional fuel assemblies, each occupying a 45 degree segment of a cylindrical annulus. Each fuel assembly consists of 24 circumferential plates. The fuel is uranium-aluminide dispersion, UAl_x, with uranium enriched to approximately 93% ^{235}U. The core is surrounded by two concentric annulus reflectors. The beryllium metal inner reflector annulus is 6.88 cm thick. The outer reflector annulus is 22.58 cm thick graphite canned in aluminum. The graphite reflector region was designed for large sample irradiations, and housed the natural UO_2 fuel samples during the thermal neutron irradiation. Table 7 shows the reactor characteristics of the MURR core obtained from the 2006 MURR SAR.[50]

Table 7: Summary of MURR reactor parameters.[50] Reprinted with permission from J.M. Osborn *et al*., 2018

Parameter	Value
Reactor Power (MWth)	10
Reactor Core Geometry	Annular
Innermost Fuel Plate Center Radius (cm)	7.099
Outermost Fuel Plate Center Radius (cm)	14.694
Fuel Material	Uranium-aluminide dispersion (UAl_x)
Fuel Enrichment	93% ^{235}U
Fuel Assembly Cladding	Aluminum
Number of Sectional Fuel Assemblies	8
Fuel Plates Per Assembly	24
Fuel Plate Thickness (mm)	1.27
Coolant	Light Water
Control Blade Material	Boral
Control Blade Thickness (mm)	6.35
Inner Reflector Material	Beryllium
Inner Reflector Thickness (cm)	6.88
Outer Reflector Material	Graphite
Outer Reflector Thickness (cm)	22.58

5.3 Description of the Irradiation at MURR

The three discs were housed in an 1100 aluminum alloy irradiation capsule approximately 3 cm in diameter, and irradiated in the graphite region surrounding the MURR core. The MURR operators provided information on the irradiation location and irradiation history of the fuel samples. The sample irradiation location was reported as 36.2 cm axially above the core center and radially 27.9 cm from the core center. During a typical week, the MURR will operate at full power for approximately 6.5 days, followed by a shutdown of approximately 12 hours for refueling before resuming

operation. The irradiation location allotted to the natural UO_2 fuel samples was also used for other MURR irradiations. Thus, between planned shutdowns, unplanned shutdowns, and shuffling in the irradiation location, the samples underwent a complex irradiation history. The total reported irradiation history consisted of 33 irradiations totaling 111.9 effective full-power days (EFPDs), over the course of 126.3 days which concluded on April 25, 2017. The specific fuel sample irradiation history is contained in Table 8. The irradiation capsule, post-irradiation, is shown in Fig. 20. The irradiation was not performed in a manner that would allow the specific discs to be identified after irradiation. Post-irradiation the fuel discs were arbitrarily denoted as disc 'A', 'B', and 'C'. The true location of the control blades throughout the irradiation was an unknown parameter. However, for the simulation a representative control blade position was determined, details of which are described in the following section.

Figure 20: The irradiation capsule housing three wrapped fuel discs following the irradiation at MURR.

Table 8: Fuel sample irradiation history during the experimental irradiation at MURR.

Irradiation Start Date & Time	Irradiation End Date & Time	Hours Irradiated
12/20/2016 0:35	12/26/2016 2:00	145.42
12/26/2016 14:54	1/2/2017 2:00	155.10
1/2/2017 14:12	1/8/2017 22:44	152.53
1/9/2017 16:43	1/10/2017 8:27	15.73
1/10/2017 17:45	1/11/2017 9:55	16.17
1/11/2017 10:12	1/14/2017 15:12	77.00
1/14/2017 15:26	1/16/2017 2:00	34.57
1/16/2017 19:33	1/17/2017 21:30	25.95
1/18/2017 5:32	1/23/2017 2:00	116.47
1/23/2017 19:48	1/30/2017 2:00	150.20
1/30/2017 22:15	2/6/2017 2:00	147.75
2/6/2017 19:09	2/7/2017 22:52	27.72
2/8/2017 8:34	2/8/2017 9:58	1.40
2/8/2017 10:18	2/11/2017 1:19	63.02
2/11/2017 1:34	2/13/2017 2:00	48.43
2/13/2017 16:03	2/15/2017 9:57	41.90
2/15/2017 10:12	2/18/2017 1:12	63.00
2/18/2017 1:21	2/20/2017 2:00	48.65
2/20/2017 15:23	2/27/2017 2:00	154.62
2/27/2017 18:05	3/6/2017 2:00	151.92
3/6/2017 18:04	3/13/2017 2:00	150.93
3/13/2017 15:24	3/15/2017 9:58	42.57
3/15/2017 10:07	3/18/2017 1:08	63.02
3/18/2017 1:29	3/20/2017 2:00	48.52
3/21/2017 0:18	3/27/2017 2:00	145.70
3/27/2017 19:29	4/3/2017 2:00	150.52
4/3/2017 16:45	4/10/2017 2:00	153.25
4/10/2017 20:24	4/12/2017 10:06	37.70
4/12/2017 10:33	4/15/2017 1:37	63.07
4/15/2017 1:48	4/17/2017 2:00	48.20
4/18/2017 0:31	4/20/2017 14:49	62.30
4/20/2017 22:47	4/24/2017 2:00	75.22
4/25/2017 1:48	4/25/2017 7:52	6.07

5.4 MURR Model and Burnup Simulation Development

A computational model of the MURR core was developed using MCNP6 in order to perform burnup simulations to be representative of the experimental irradiation performed in the MURR facility. The MCNP model of the MURR core was based on reactor characteristics found in the 2006 MURR SAR.[50] Due to the large computational cost of full core simulations, a one-eighth core model was developed. This was acceptable due to the eightfold symmetry of the MURR core. The one-eighth core model featured a 45 degree segment of the MURR core, containing one full fuel assembly, with reflecting boundary conditions on the 0 degree and 45 degree planes. Additionally to improve statistics, the three average fuel discs simulated in MCNP were treated as a single material. Upon receiving the three neutron irradiated natural UO_2 samples, gamma spectrometry measurements were performed to calculate the burnup. For the simulation, an iterative process was used to determine the control blade height which would result in the flux level required to match the measured burnup. To do so, the bottom of the control blade was fixed at 24.5 cm above axial center. Fig. 21 illustrates a radial cross section of the one-eighth MURR core model developed in MCNP, and an axial cross section of the one-eighth MURR core model with the sample irradiation location shown.

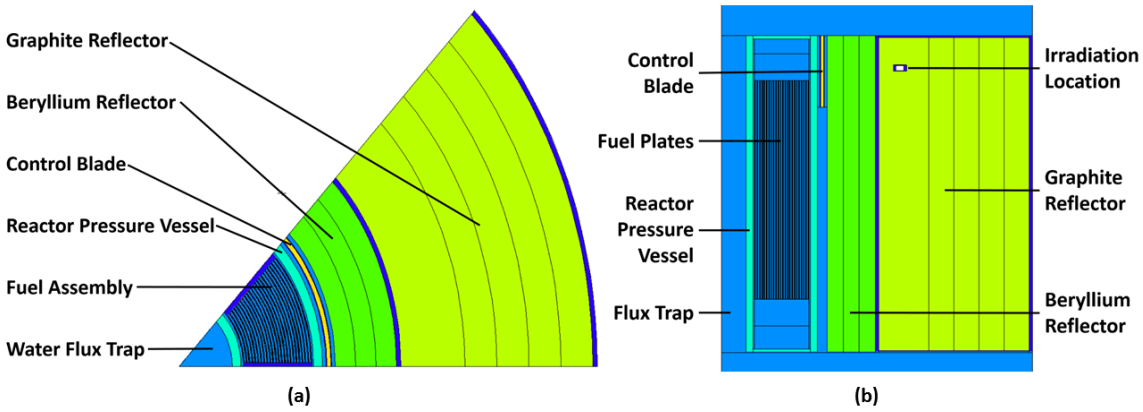

Figure 21: (a) A radial cross section of one-eighth MURR core model in MCNP and (b) an axial cross section of one-eighth MURR core model showing the sample irradiation and control blade locations. Reprinted with permission from J.M. Osborn *et al.*, 2018

A preliminary simulation was performed, in which the core fuel material was burned for a 6.5 day full power week, in order to establish the ^{135}Xe equilibrium concentration. During this simulation the neutron flux in the irradiation location was calculated, and as expected, the neutron flux magnitude and spectrum in the irradiation location was not affected by the varying ^{135}Xe concentration within the core fuel. The process by which MCNP normalized the neutron flux magnitude with the given power level resulted in the total neutron flux magnitude remaining constant with changing ^{135}Xe concentration. Due to the proximity of the irradiation location relative to the core, the neutron flux within the irradiation location was thermalized by the beryllium and graphite reflectors. As a result, the changing neutron spectrum within the core due to the buildup of ^{135}Xe was not observed in the irradiation location. With the ^{135}Xe equilibrium concentration added to the core fuel material, the core fuel was not depleted further during the burnup simulation of the natural UO_2 samples. This was done to avoid the

need to account for depletion of the core fuel, avoid adjusting the height of the control blade, avoid refueling, decrease the computational cost of the simulations, and to ensure that the samples experienced a constant neutron flux for the entirety of the reported irradiation history. Thus the natural UO_2 samples were the only material in which burnup was tracked using the CINDER-90 module of MCNP.

In order to keep the relative MCNP stochastic error in the important neutron reaction rates leading to production and loss of the isotopes of interest to less than 10% and efficiently allocate the computing resources of a multi-core cluster, the simulation was performed with 10^6 particles per cycle and 250 active cycles for every burnup time step (33 full power, 32 intermittent zero power steps, and decay to the measurement dates).

6. EXPERIMENTAL PROCEDURES*

Following completion of the experimental irradiation at MURR, the three irradiated fuel discs were subject to a preliminary analysis shortly after being received. The work presented here focuses on the material characterization performed approximately five month after irradiation completed. The characterization of the irradiated fuel samples included gamma and mass spectrometry measurements to determine fuel burnup, as well as radioactive and stable fission product and plutonium isotopic concentrations.

6.1 Gamma Spectrometry Measurements of MURR Irradiated Sample

There are multiple technologies used for gamma spectrometry measurements with the most common detectors being sodium iodide (NaI) scintillation detectors and high-purity germanium (HPGe) semiconductor detectors. For the gamma energy resolution desired for the isotopic characterization performed during this study an HPGe detector was used. The gamma spectrometry measurements for this study were performed using a Canberra Model GC4018 Standard Electrode Coaxial HPGe detector cooled with liquid nitrogen. Prior to each gamma measurement, an energy and efficiency calibration was conducted. A NIST traceable liquid ^{152}Eu source with an activity of 371 nCi (497 ± 0.5 nCi on February 15, 2012) was used as the calibration source. The ^{152}Eu source emits gammas with a wide range of energies, useful for fitting a calibration

* Reprinted with permission from "Computational and experimental forensics characterization of weapons-grade plutonium produced in a thermal neutron environment" by J.M. Osborn *et al.*, 2018. *Nucl. Eng Technol.*, 50, 820-828, Copyright 2018 by Korean Nuclear Society.

curve with a single calibration source. Table 9 provides the gamma energies and yields emitted from the ^{152}Eu source used for constructing the calibration curve. An example calibration curve is shown in Fig. 22, with the data points from the ^{152}Eu calibration source and the resulting third degree polynomial fit efficiency curve.

Table 9: Gamma energies and yields emitted from ^{152}Eu calibration source.[51]

Energy (keV)	Yield (%)
39.82	97.7
45.35	11.0
46.64	3.3
121.78	28.6
244.70	7.6
344.28	26.5
367.79	0.9
411.12	2.2
443.97	2.8
688.67	0.9
778.90	12.9
867.38	4.2
964.08	14.6
1005.27	0.6
1085.87	10.2
1089.74	1.7
1112.07	13.6
1212.95	1.4
1299.14	1.6
1408.01	21.0

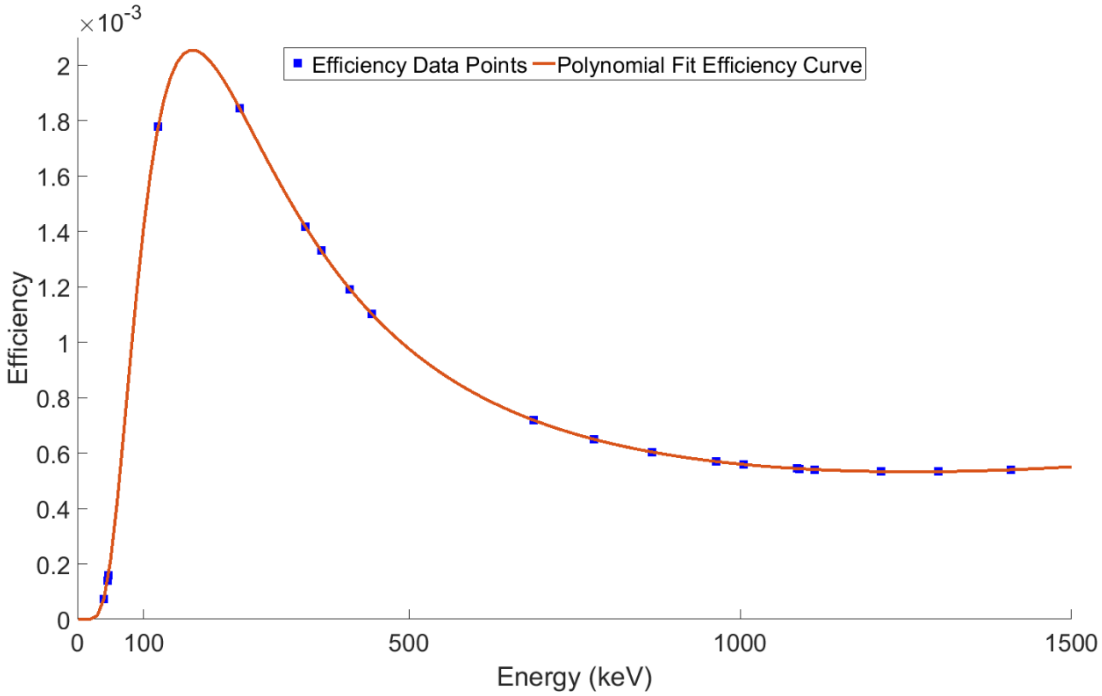

Figure 22: Example of the third degree polynomial fit efficiency curve fitted to the ^{152}Eu calibration source measurements.

On October 2, 2017, the irradiation capsule was opened and gamma spectrometry measurements of individual fuel discs were conducted to determine the fuel sample burnup indirectly by measuring the ^{137}Cs activity within each fuel disc. Each fuel sample was measured at distance of 1 m from the HPGe spectrometer face, as seen in Fig. 23, resulting in a dead time of 52%.

Figure 23: The initial gamma measurement setup for determining the burnup of each fuel disc.

Following the initial gamma spectrometry measurements a single fuel disc, disc C, was chosen for dissolution in order to allow more precise gamma and mass spectrometry measurements. The irradiated fuel disc was transferred to a round bottom flask where approximately 4.5 mL of 8 M nitric acid (HNO_3) was added and heated until dissolution. The round bottom flask was connected to a cold trap via a Schlenk line and vacuum pump for the purpose of collecting volatile fission product gasses. The dissolution setup is shown in Fig. 24 including the round bottom flask, heating mantle, Schlenk line, cold trap, and vacuum pump. The dissolution setup was prepared by Kevin J. Glennon and the fuel disc dissolution was performed by Dr. Jonathan D. Burns. The dissolution produced an approximately 4.5 mL solution, as seen in Fig. 25, containing approximately 95% of the original disc. The approximately 95% recovery was determined by comparing the gamma spectrometry measured ^{137}Cs activity of disc C prior to dissolution and the recovered solution post-dissolution.

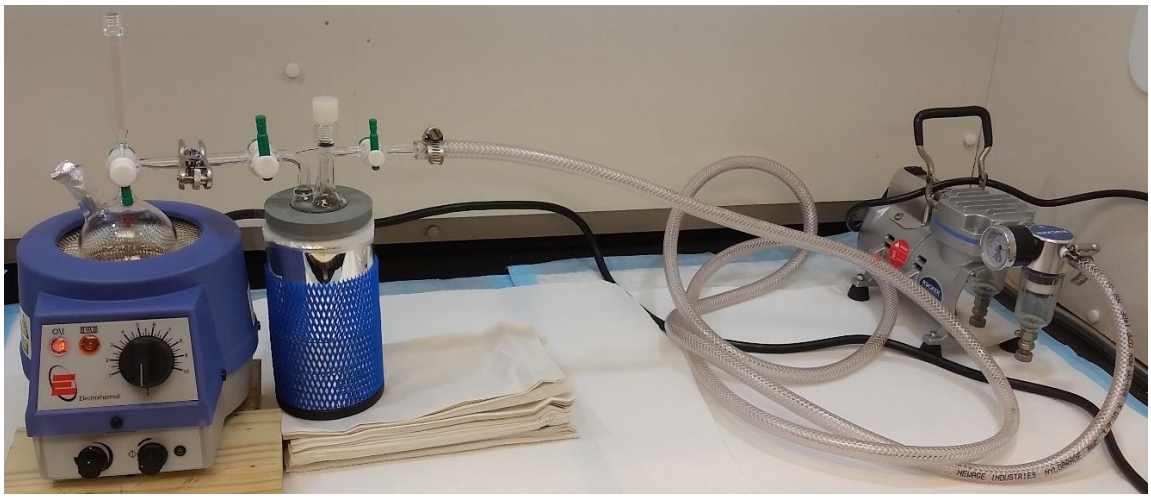

Figure 24: Setup for the dissolution of the irradiated natural UO_2 fuel disc.

Figure 25: ~4.5 mL solution containing approximately 95% of the dissolved fuel disc.

On October 13, 2017 an aliquot solution containing 1% of the dissolved disc was used for more precise gamma spectrometry measurements to determine the fission product

concentrations in the original sample. In taking a 1% aliquot of the solution, gamma spectrometry measurements could be performed within a lead shielded cave, with minimal background and at a closer distance, without saturating the detector. Measurements were performed with the same Canberra Standard Electrode Coaxial HPGe detector. Both the 1% aliquot and the HPGe detector were surrounded by a lead cave, as seen in Fig. 26. The 1% aliquot solution was measured at a distance of 26 cm from the detector face with a dead time of 6%. The isotopes measured using gamma spectrometry included ^{95}Zr, ^{103}Ru, ^{134}Cs, ^{137}Cs, ^{141}Ce, and ^{144}Ce.

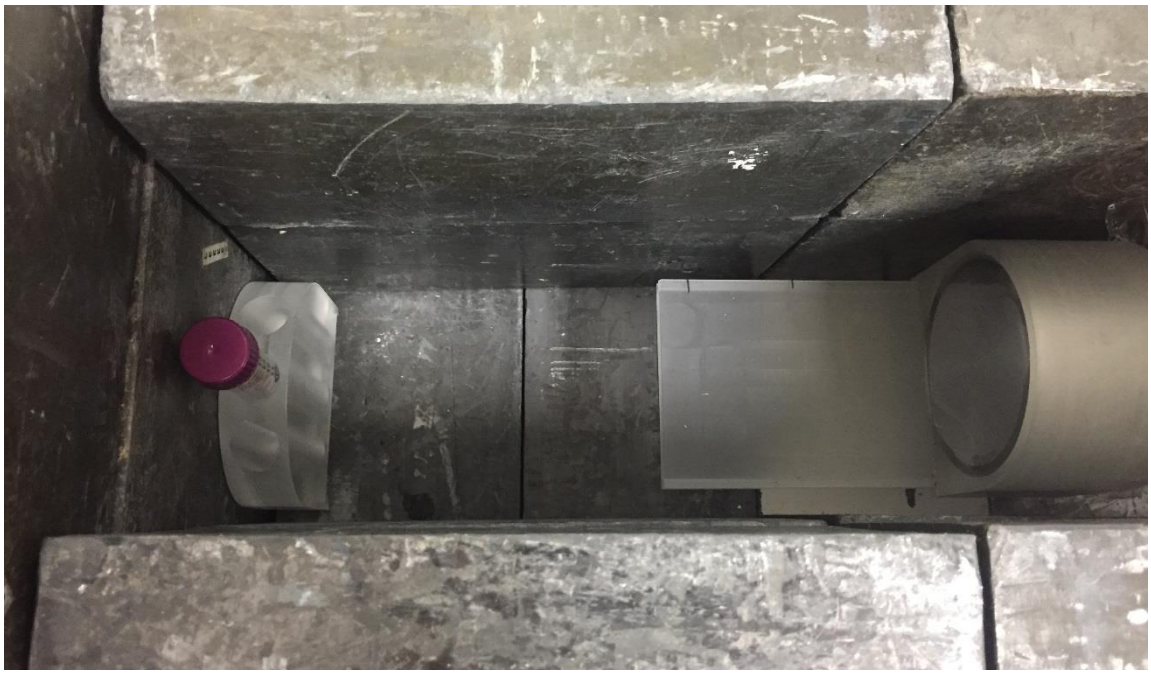

Figure 26: The gamma spectrometry measurement setup with the 1% aliquot, sample holder, and HPGe detector within a lead cave.

6.2 Mass Spectrometry Measurements of MURR Irradiated Sample

Mass spectrometry was utilized to measure plutonium and stable fission product isotope concentrations in the irradiated fuel sample. Inductively coupled plasma mass spectrometry (ICP-MS) measurements were performed at Texas A&M University using a Thermo Fisher Scientific iCAP RQ spectrometer. An image of the mass spectrometer used is shown in Fig. 27. The mass spectrometry aliquots of the irradiated fuel samples were prepared by Kevin Glennon, and the mass spectrometry measurements were carried out by Kevin Glennon and Dr. Brent V. Miller.

Figure 27: The Thermo Fisher Scientific iCAP RQ ICP-MS used for mass spectrometry measurements.

On October 19, 2017 mass spectrometry measurements of the previously characterized[13] HFIR irradiated DUO_2 fuel sample were first performed in order to obtain the intra-element isotope ratio values needed for the maximum likelihood analysis part of the methodology developed. On March 9, 2018 mass spectrometry measurements of the MURR irradiated natural UO_2 fuel sample were first performed in order to characterize the irradiated material and to obtain the intra-element isotope ratio values needed for the maximum likelihood analysis. Three aliquots with 1% of the dissolved disc were subsequently prepared for mass spectrometry by dilution into 5 mL of ultra-pure 1% HNO_3 purchased as Omni-Trace Ultra Nitric Acid from MilliporeSigma (Burlington, Massachusetts, USA). These three aliquots were used to quantify the masses of plutonium and fission products. Three more aliquots containing 0.01% of the dissolved disc were prepared the same way to quantify the mass of uranium. Calibration standards were prepared for Cs, Ce, Sm, Eu, and U at concentrations from 0.01 ppb to 500 ppb using 1,000 ppm ICP-MS standards purchased from BDH Chemicals (Radnor, Pennsylvania, USA). Each aliquot was measured multiple times to take an average and standard deviation. The results from the first three 1% aliquots were then averaged together to determine the concentration of Pu, Cs, Ce, Nd, Sm, and Eu. The measurement errors of the averages were determined by fully propagating the errors of the individual measurements. The average concentration of U in the three 0.01% aliquots was used to determine the concentration of U in each of the three 1% aliquots, such that the fission products could be normalized to U. The known mass of U in the total pellet

was then used to determine the total masses of Pu, Cs, Ce, Nd, Sm, and Eu in the entire disc.

Of the fifteen isotopes which comprise the ten intra-element isotope ratios utilized in the forensics methodology developed for this study, we knew two isotopes would have isobaric interferences which mass spectrometry is unable to resolve. An isobaric interference exists in mass chain 137 amu between the isotope of interest, ^{137}Cs, and ^{137}Ba, and similarly in mass chain 150 amu between the isotope of interest, ^{150}Sm, and ^{150}Nd. Two techniques were employed to address this issue. First was a fissiogenic ratio based on the MCNP simulation results to delineate the contribution of a desired isotope. The fissiogenic ratio correction was the sole method used during the characterization of the MURR irradiated material, contained in Section 8. The fissiogenic ratio was also used to correct the ^{137}Cs contribution to the mass chain 137 isobar for the intra-element isotope ratio employed in the maximum likelihood analysis. This is a small correction as the majority (>95%) of the mass 137 isobar is ^{137}Cs given the irradiation or decay time is not large compared to the half-life of ^{137}Cs. The direct fission yield of ^{137}Ba is negligible, as well as the radiative capture on ^{136}Ba. Thus the primary production path of ^{137}Ba is from the decay of ^{137}Cs.

The second technique was to perform a chemical separation of the element of interest prior to measurement by mass spectrometry. This approach was employed to measure the ^{150}Sm/^{149}Sm ratio for both irradiated samples. Cation exchange column chromatography has the ability to chemically separate the lanthanide elements. All lanthanides are trivalent cations in solution.[52] With increasing atomic number, the 4f

electron shell is being filled. This is not the outermost shell, thus the increasing atomic number decreases the ionic radius and increases the charge density. This phenomenon is known as the lanthanide contraction. The increased charge density attracts more water molecules to bond, creating a larger hydration sphere.[52] By using an eluent which interacts more strongly to cations with a larger hydration sphere, a chemical separation of the lanthanides can be achieved. Column chromatography was used to separate Sm from Nd. The $^{150}Sm/^{149}Sm$ ratio was determined within the Sm elution peak, which contained no ^{150}Nd, by mass spectrometry. The column chromatography was performed by Kevin Glennon.

7. MCNP SIMULATION RESULTS*

The first result analyzed for each reactor model simulation detailed in Section 3.4 was a neutron flux spectrum and magnitude. A 238-energy-group neutron spectrum was calculated using MCNP, and displayed in Fig. 28. Table 10 contains the neutron flux calculated within the fuel region of interest for all library reactor models at the beginning of the MCNP burnup simulations. The relative stochastic error on the neutron flux magnitude was less than 1% for each simulation.

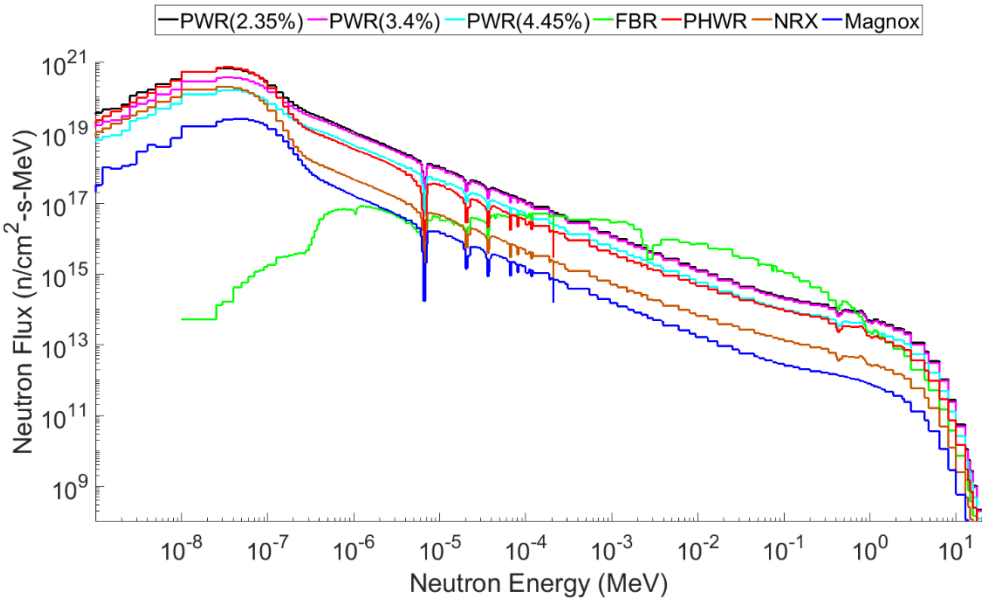

Figure 28: A comparison of the 238-energy-group neutron flux per MeV for the power reactors contained in the reactor library, from MCNP simulation.

* Reprinted with permission from "Computational and experimental forensics characterization of weapons-grade plutonium produced in a thermal neutron environment" by J.M. Osborn *et al.*, 2018. *Nucl. Eng Technol.*, 50, 820-828, Copyright 2018 by Korean Nuclear Society.

Table 10: MCNP calculated neutron flux at the beginning of burn for the library reactor models.

Reactor Model	Total Flux (n/cm^2-s)	Thermal Flux E < 0.5 eV (n/cm^2-s)	Fast Flux E > 0.1 MeV (n/cm^2-s)
PWR (2.35%)	4.09×10^{14}	7.09×10^{13}	1.86×10^{14}
PWR (3.4%)	3.47×10^{14}	4.45×10^{13}	1.66×10^{14}
PWR (4.45%)	1.74×10^{14}	2.01×10^{13}	8.68×10^{13}
FBR	5.79×10^{14}	6.50×10^{9}	2.17×10^{14}
PHWR	1.75×10^{14}	6.04×10^{13}	6.51×10^{13}
NRX	3.27×10^{13}	1.58×10^{13}	9.83×10^{12}
Magnox	8.30×10^{12}	3.32×10^{12}	2.67×10^{12}
HFIR	1.60×10^{15}	5.86×10^{12}	8.03×10^{14}
MURR	5.06×10^{13}	3.15×10^{13}	4.62×10^{12}

7.1 Comparison of the Experimental Irradiation at MURR to Natural Uranium Fueled Thermal Reactors

The first step in verifying that the plutonium produced in the experimental irradiation at MURR was a suitable surrogate to plutonium produced in the natural uranium fueled thermal neutron reactor types identified, was to compare the neutron flux spectra and magnitude obtained from the MCNP simulations. The 238-energy-group neutron flux spectra, within the fuel, obtained from the MCNP simulations of the natural UO_2 fuel irradiation at MURR, compared with the NRX, PHWR, and Magnox type reactors are shown in Fig. 29.

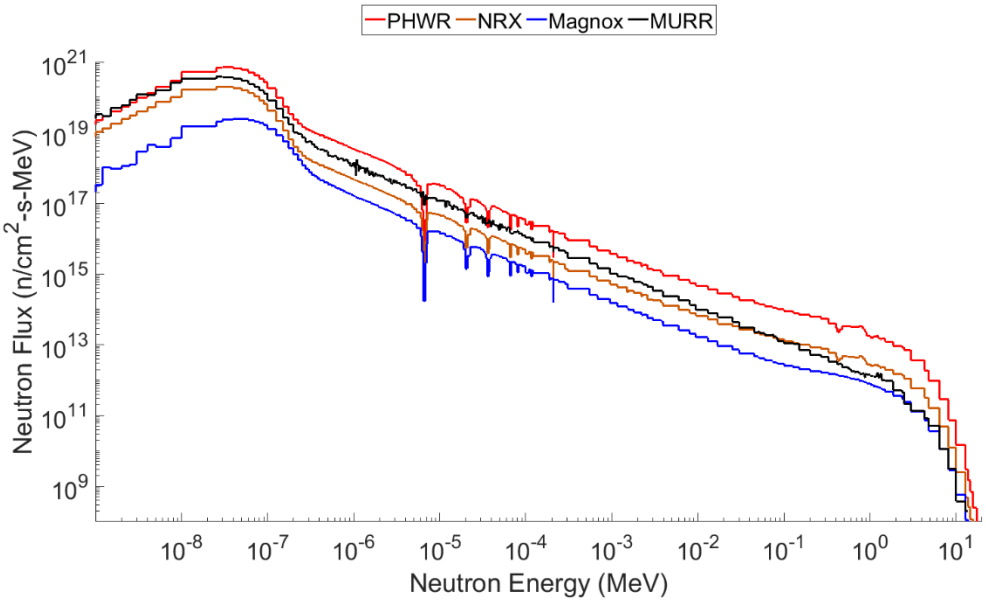

Figure 29: A comparison of the neutron flux per MeV for the three natural uranium production reactors to the experimental irradiation at MURR from MCNP simulations. Reprinted with permission from J.M. Osborn *et al*., 2018

The important feature to note from Fig. 29 is the similarity of the thermal neutron peaked shape of the neutron flux spectra for each reactor simulation. Visible in Fig. 29 are the multiple dips in the neutron flux from approximately 6 – 100 eV. This phenomenon is known as self-shielding and is a depression in the neutron flux corresponding to the ^{238}U neutron absorption cross-section resonances. Evident in Fig. 29 is the neutron flux depressions are either non-existent or significantly reduced in the spectrum for the experimental irradiation at MURR. This is due to the fuel disc samples irradiated at MURR being small and dilute enough that the self-shielding effect is not present. This difference in the neutron flux for the experimental irradiation at MURR could have a slight effect on resulting isotopics. The differences in the neutron

flux magnitudes amongst the simulations can be noted in both Fig. 29 and Table 10. For a given level of burnup, the neutron flux magnitude and irradiation time will be inversely related. Thus, the neutron fluence, which is defined as the time integral of the neutron flux,[53] will be the same for reactors having similar flux shapes at a given burnup. This is significant as the production of most isotopes is dependent on the neutron fluence rather than the neutron flux.

Next, a direct comparison of the simulated fission product and actinide inventories was made. This comparison was done by taking the plutonium vector and fission product concentrations predicted by the MCNP simulation of the experimental irradiation at MURR, and comparing them to the corresponding MCNP predictions of concentrations in the natural uranium production reactors at the same burnup level. The simulation of the sample irradiation at MURR predicted a burnup of 0.96 GWd/MTU with a stochastic relative error of 0.086%, obtained by propagating total fission reaction rate errors through the burnup simulation. With no simulation burnup steps at exactly this value for the NRX, PHWR, and Magnox models, the material compositions at a burnup level of 0.96 GWd/MTU for these models were attained using linear interpolation between predicted isotopics at neighboring burnup values. Table 11 provides the MCNP predicted plutonium vectors for each simulation at a burnup of 0.96 GWd/MTU. The plutonium produced from the natural uranium production reactors are similar to that which was produced in the simulation of the experimental irradiation at MURR, with the ^{239}Pu percentage of the plutonium vector being within 2%.

Table 11: Comparison of the plutonium vector predicted by MCNP simulations at a burnup of 0.96 GWd/MTU. Reprinted with permission from J.M. Osborn *et al*., 2018

Isotope	MURR	PHWR	NRX	Magnox
^{238}Pu	<0.01%	<0.01%	<0.01%	0.01%
^{239}Pu	95.74%	95.77%	95.76%	94.13%
^{240}Pu	4.05%	3.98%	4.05%	5.46%
^{241}Pu	0.21%	0.24%	0.18%	0.39%
^{242}Pu	<0.01%	0.01%	<0.01%	0.01%

The fission product isotopes of interest in the forensics methodology developed are contained in Table 12. For each simulation and isotope of interest, the isotope concentration normalized to initial uranium is presented at 0.96 GWd/MTU of fuel burnup. A ratio of the isotopic concentrations in each production reactor simulation to that in the MURR simulation is calculated for ease of direct comparison. The simulation predicted values are for the material immediately after irradiation. As a result, contributions from short-lived precursors are not included in the simulations. Thus the masses of short-lived precursors have been summed with the isotopes of interest to represent the concentration at a later measurement date.

Table 12: Comparison of the concentrations of fission products including short-lived precursors as predicted by MCNP simulations at a burnup of 0.96 GWd/MTU. Reprinted with permission from J.M. Osborn *et al*., 2018

Isotope	MURR (g/gU)	PHWR (g/gU)	NRX (g/gU)	Magnox (g/gU)	PHWR / MURR	NRX / MURR	Magnox / MURR
^{133}Cs	3.76×10^{-5}	3.64×10^{-5}	3.77×10^{-5}	3.73×10^{-5}	0.97	1.00	0.99
^{134}Cs	1.67×10^{-7}	1.49×10^{-7}	1.56×10^{-7}	1.37×10^{-7}	0.89	0.93	0.82
^{135}Cs	9.84×10^{-6}	4.57×10^{-6}	1.25×10^{-5}	3.11×10^{-5}	0.46	1.27	3.16
^{137}Cs	3.61×10^{-5}	3.57×10^{-5}	3.58×10^{-5}	3.40×10^{-5}	0.99	0.99	0.94
^{136}Ba	1.15×10^{-7}	6.70×10^{-8}	8.09×10^{-8}	1.22×10^{-7}	0.58	0.70	1.06
^{138}Ba	3.89×10^{-5}	3.88×10^{-5}	3.91×10^{-5}	3.89×10^{-5}	1.00	1.00	1.00
^{149}Sm	6.55×10^{-7}	8.00×10^{-7}	5.13×10^{-7}	3.50×10^{-7}	1.22	0.78	0.53
^{150}Sm	6.36×10^{-6}	6.13×10^{-6}	6.48×10^{-6}	6.54×10^{-6}	0.96	1.02	1.03
^{152}Sm	3.84×10^{-6}	3.69×10^{-6}	3.81×10^{-6}	3.71×10^{-6}	0.96	0.99	0.97
^{153}Eu	1.29×10^{-6}	1.28×10^{-6}	1.22×10^{-6}	1.31×10^{-6}	0.99	0.95	1.02
^{154}Eu	4.59×10^{-8}	4.34×10^{-8}	4.66×10^{-8}	4.77×10^{-8}	0.95	1.02	1.04

For most of the isotopes of interest, Table 12 demonstrates great agreement in predicted fission product concentrations. All isotopes agree well (mostly within 10%) with the exceptions of ^{135}Cs, ^{136}Ba, and ^{149}Sm. This variation in predicted concentrations between reactors can be understood by investigating the production mechanisms of each isotope as discussed below.

As demonstrated by Hayes and Jungman,[54] there is a relationship between the ^{135}Cs/^{137}Cs ratio and the thermal flux magnitude. Since the concentration of ^{137}Cs is proportional to burnup, the ^{135}Cs/^{137}Cs ratio becomes synonymous with the concentration of ^{135}Cs for a given burnup. The dependency of ^{135}Cs on the flux magnitude stems from the competition between the decay of ^{135}Xe to ^{135}Cs, with a 9.14 hour half-life, and the neutron capture on ^{135}Xe creating ^{136}Xe, with a thermal cross section of ~2.6×10^6 barns. For reactor systems with a low thermal flux, the ^{135}Xe will have the ability to decay to ^{135}Cs, thus increasing the concentration of ^{135}Cs. Conversely, reactor systems with a high thermal flux will have relatively more neutron captures on ^{135}Xe, resulting in a decreased ^{135}Cs concentration. This behavior for the ^{135}Cs concentration being inversely related to the thermal flux magnitude is seen in Table 12. The largest concentration of ^{135}Cs is produced in the Magnox reactor which has the lowest thermal flux magnitude as per Table 9.

The concentration of ^{136}Ba behaves with a similar trend to that of ^{135}Cs. The independent fission yield of ^{136}Ba is approximately three orders of magnitude lower than the cumulative fission yield, meaning that the primary production mechanism of ^{136}Ba is from the decay of ^{136}Cs with a half-life of approximately 13.16 days. ^{136}Cs is blocked by

the effectively stable ^{136}Xe, thus ^{136}Cs is produced as a direct fission product and from the neutron capture on ^{135}Cs. ^{136}Cs has a neutron capture cross-section in the tens of barns range for thermal neutron energies. Reactor systems with a higher thermal neutron flux will have more neutron captures on ^{136}Cs, thus decreasing the amount that decays to ^{136}Ba. Again, the ^{136}Ba concentration is inversely related to the thermal flux magnitude with the highest concentration found in the Magnox reactor.

Conversely, ^{149}Sm exhibits a direct relationship with the magnitude of the thermal neutron flux. The dominant production route for ^{149}Sm is from beta-decay of mass chain 149 precursors. For a given reactor system, the concentration of ^{149}Sm reaches an equilibrium value, and is independent of power level or flux magnitude.[55] However, ^{149}Pm, the radioactive precursor to ^{149}Sm, is produced as a fission product with the concentration directly related to the flux magnitude.[55] With a half-life of 53.1 hours, it is safe to assume that all the ^{149}Pm will have time to fully decay into ^{149}Sm prior to a measurement. Therefore a measurement of ^{149}Sm will be the sum of both ^{149}Pm and ^{149}Sm and is thus related to the flux magnitude. This behavior is seen in Table 12, with the relative ^{149}Sm concentrations being directly related to the relative flux magnitudes.

The results contained in Tables 11 and 12 positively support the objective of the simulation comparison. For this study, an agreement in the plutonium and fission product concentrations predicted by the simulations serve to verify the similarities of the natural uranium production reactors and the experimental irradiation of natural UO_2 samples in MURR. Most of the isotopes of interest agreed within 10% among the

simulations. The relationship between thermal flux magnitude and the isotopes of ^{135}Cs, ^{136}Ba, and ^{149}Sm assists in understanding the four intra-element isotope ratios containing these isotopes (^{135}Cs/^{137}Cs, ^{136}Ba/^{138}Ba, ^{150}Sm/^{149}Sm, ^{152}Sm/^{149}Sm) and their contribution to resolving reactor type.

8. COMPARISON OF EXPERIMENTAL MEASUREMENTS AND MCNP SIMULATION FOR THE NATURAL UO_2 IRRADIATION AT MURR*

8.1 Determination of Fuel Burnup from ^{137}Cs Concentration Measurements

The initial gamma spectrometry measurement performed on the full fuel discs prior to dissolution were done to calculate the burnup via the ^{137}Cs activity. The measured activity for ^{137}Cs, and other nuclides of interest, were calculated using Eq. 19 and the detector efficiency, an example of which is shown in Fig. 22.

$$A_n = \frac{CPS_n}{\varepsilon_\gamma * Y_\gamma} \tag{19}$$

Where:

A_n = the activity of nuclide n

CPS_n = the dead time corrected count rate (counts per second) in the full-energy peak of the gamma-ray, γ, from nuclide n

ε_γ = the detector efficiency at the energy of gamma-ray γ

Y_γ = the yield, or branching ratio, of gamma-ray, γ, from nuclide n

Table 13 provides the count rate in the 661.7 keV peak, the measured ^{137}Cs activity, and the activity decay corrected for the 160 days between the measurement date and the end of irradiation for each fuel disc. The error in the measured activities includes statistical errors in the measurement, background, and efficiency calibration counts.

---

* Reprinted with permission from "Computational and experimental forensics characterization of weapons-grade plutonium produced in a thermal neutron environment" by J.M. Osborn *et al.*, 2018. *Nucl. Eng Technol.*, 50, 820-828, Copyright 2018 by Korean Nuclear Society.

Table 13: Measured ^{137}Cs activity within each fuel disc.

Fuel Disc	CPS (Live)	Measured ^{137}Cs Activity (Bq)	End of Irradiation Decay Corrected ^{137}Cs Activity (Bq)
A	69.86	$(1.654 \pm 0.025) \times 10^6$	$(1.670 \pm 0.025) \times 10^6$
B	70.25	$(1.663 \pm 0.025) \times 10^6$	$(1.680 \pm 0.025) \times 10^6$
C	71.66	$(1.696 \pm 0.025) \times 10^6$	$(1.713 \pm 0.026) \times 10^6$

The ^{137}Cs activity was converted to the number of ^{137}Cs atoms by dividing the activity by the decay rate for ^{137}Cs, λ_{137Cs}. The burnup for each fuel disc was calculated using Eq. 20.

$$Bu = \frac{N_{137Cs} * Q}{Y_{137} * U} \tag{20}$$

Where:

Bu = burnup

N_{137Cs} = the number of ^{137}Cs atoms

Q = the average energy released per fission

Y_{137} = the cumulative fission yield for ^{137}Cs

U = the mass of uranium

The average mass of uranium in the UO_2 fuel discs was approximately 14.52 mg, or 1.452×10^{-8} MT. By assuming an average energy released per fission as 202 ± 5 MeV and a ^{137}Cs cumulative fission yield of 6.221% ± 0.069%[56], the burnup was calculated with Eq. 20. Table 14 compares the experimentally determined sample burnup calculated via measured ^{137}Cs activity, and the average predicted burnup by the MCNP simulation of the experimental irradiation at MURR. The measured burnup error contains the

propagated errors in the measured activity, variation in the average mass of uranium, uncertainty in the average energy released per fission, and the uncertainty in the fission yield. The simulated burnup stochastic error was obtained from propagating the total fission reaction rate errors through the MCNP burnup simulation. Table 14 indicates an excellent agreement in the measured burnup, and the MCNP simulated burnup.

Table 14: Comparison of the experimentally determined burnup via ^{137}Cs activity and the MCNP simulated burnup.

Fuel Disc	Measured Burnup (GWd/MTU)	Measured Burnup Error	Simulated Burnup (GWd/MTU)	Simulated Burnup Stochastic Error	S/E[a]
A	0.949	3.3%	0.960	0.086%	1.01 ± 0.03
B	0.954	3.3%	0.960	0.086%	1.01 ± 0.03
C	0.973	3.3%	0.960	0.086%	0.99 ± 0.03

[a] S/E = simulation/measurement

8.2 Gamma Spectrometry Results

Following the dissolution of pellet C and aliquot preparation, characterization of the irradiated sample was continued with precise gamma spectrometry measurements of six isotopes (^{95}Zr, ^{103}Ru, ^{134}Cs, ^{137}Cs, ^{141}Ce, and ^{144}Ce) in the 1% aliquot of the nitric acid solution. The measurement data contained in Table 15 and Eq. 19 were used to calculate the activity for each isotope's gamma energy peaks, the average of which is the measured activity also contained in Table 15.

Table 15: Gamma measurement data used to determine the activities of selected isotopes.

Isotope	Gamma Energy (keV)	Gamma Yield (%)	Detector Efficiency (%)	Count Rate (CPS)	Activity in Solution of Each Gamma Energy (Bq)	Measured Activity (Bq)
^{95}Zr	724.2	44.17	0.069	7.28×10^{1}	2.39×10^{5}	
	756.7	54.00	0.066	8.74×10^{1}	2.43×10^{5}	2.41×10^{5}
^{103}Ru	497.1	90.90	0.098	4.12×10^{1}	4.61×10^{4}	
	610.3	5.75	0.080	2.18×10^{0}	4.72×10^{4}	4.67×10^{4}
^{134}Cs	563.2	8.65	0.087	1.05×10^{-1}	1.41×10^{3}	
	569.3	15.38	0.086	1.33×10^{-1}	1.01×10^{3}	
	604.7	97.62	0.081	7.39×10^{-1}	9.36×10^{2}	
	795.9	85.53	0.064	5.68×10^{-1}	1.04×10^{3}	
	801.9	8.69	0.064	5.97×10^{-2}	1.08×10^{3}	
	1365.2	3.01	0.054	1.44×10^{-2}	8.92×10^{2}	1.06×10^{3}
^{137}Cs	661.7	85.10	0.074	1.02×10^{1}	1.62×10^{4}	1.62×10^{4}
^{141}Ce	145.4	48.20	0.199	3.83×10^{1}	4.00×10^{4}	4.00×10^{4}
^{144}Ce	133.5	11.09	0.190	5.89×10^{1}	2.79×10^{5}	2.79×10^{5}

For each isotope the measured activity was normalized to the activity present within the full disc by accounting for the 95% pellet recovery during dissolution and the

1% of the solution aliquot. These activities within the full disc and count rate errors are displayed in Table 16 along with the MCNP predicted activities, as well as a comparison of measured and simulated values. The simulation results in Table 16 account for the 171 days of decay between the end of irradiation and the measurement date. The count rate error is the counting error in the background-subtracted peak for each isotope, and propagated over multiple peaks, if applicable. The count rate error is not equivalent to the activity error as it does not include the error in detector efficiency at each energy or the errors in the gamma yields.

Table 16: Comparison of gamma spectrometry measured activities and simulated activities within one full fuel disc. Reprinted with permission from J.M. Osborn *et al*., 2018

Isotope	Measured Activity in Full Disc (Bq))	Count Rate (CPS) Error	Simulated Activity in Full Disc (Bq)	S/E[a]
^{95}Zr	2.54×10^7	< 0.1%	2.49×10^7	0.98
^{103}Ru	4.92×10^6	0.3%	5.62×10^6	1.14
^{134}Cs	1.12×10^5	2.2%	9.92×10^4	0.89
^{137}Cs	1.71×10^6	0.1%	1.67×10^6	0.98
^{141}Ce	4.21×10^6	0.1%	4.77×10^6	1.13
^{144}Ce	2.94×10^7	< 0.1%	3.11×10^7	1.06

[a] S/E = simulation/measurement

Table 16 shows a good agreement between the gamma spectrometry measured isotope activities and the MCNP simulation predictions, with most isotope measurements within ~10% of the predicted activity. An isotope of interest excluded

from Tables 15 and 16 was ^{154}Eu. Calculated activity results were inconsistent across the multiple ^{154}Eu gamma lines identified. The MCNP simulation predicted that the 1% aliquot solution would contain approximately 64 Bq of ^{154}Eu activity, which we have concluded is below the detectable limit when present within such an active background.

8.3 Mass Spectrometry Results

On March 9, 2018 mass spectrometry measurements of the MURR irradiated fuel sample were performed for the dual purpose of characterizing the irradiated material in addition to obtaining the intra-element isotope ratio values needed for the maximum likelihood analysis. This section contains the results for the material characterization and comparison with MCNP simulation predictions. The mass spectrometry measured intra-element ratio values are provided later in Section 9.3.

The mass spectrometry measurements performed on the three 1% and three 0.01% aliquot solutions provided data on the actinides and stable fission products normalized to the mass of uranium in the average fuel disc. Table 17 presents the total mass of plutonium within the dissolved fuel disc as measured by mass spectrometry and compared to the mass predicted by the MCNP simulation of the experimental irradiation at MURR. The stochastic error in the total plutonium mass predicted by the simulation was estimated by propagating the reaction rates and reaction rate errors for the neutron capture on ^{238}U and the fission of ^{239}Pu throughout the MCNP burnup simulation. Table 18 further compares the produced plutonium by analyzing the plutonium vector. The simulation results presented account for the 318 days of decay between the end of irradiation and the date of mass spectrometry measurements.

Table 17: Comparison of the plutonium mass measured by mass spectrometry and simulated by MCNP.

Measured Pu Mass (μg)	Measurement Error	Simulated Pu Mass (μg)	Simulated Stochastic Error	S/E[a]
20.1	5.3%	20.9	0.78%	1.04 ± 0.06

[a] S/E = simulation/measurement

Table 18: Comparison of the plutonium vector measured by mass spectrometry and simulated by MCNP. Reprinted with permission from J.M. Osborn *et al*., 2018

Isotope	Measured Pu Vector	Measured Pu Vector Relative Error	Simulated Pu Vector	S/E[a]
^{239}Pu	95.22%	0.1%	95.75%	1.01
^{240}Pu	4.55%	2.2%	4.05%	0.89
^{241}Pu	0.23%	1.9%	0.20%	0.86
^{242}Pu	<0.01%	N/A	<0.01%	N/A

[a] S/E = simulation/measurement

Tables 17 and 18 show that the simulation and measurements agree well for the total mass of plutonium produced and the plutonium vector, respectively. From Table 18 it can be seen that the S/E comparison becomes worse for higher mass plutonium isotopes. The smaller quantities of ^{240}Pu and ^{241}Pu isotopes lead to an increase in measurement error. Additionally, the increasing number of reactions involved in the concentrations of the higher mass plutonium isotopes propagates to a larger simulation error in the MCNP predictions of ^{240}Pu, ^{241}Pu, and ^{242}Pu.

Table 19 compares fission product masses as measured by mass spectrometry and predicted by MCNP simulation of the experimental irradiation at MURR. The

measured mass spectrometry response was normalized to the isotope mass (g) within the full fuel disc, 14.5 mg of U. The mass spectrometer is measuring a mass-to-charge ratio. Assuming a charge of +1 in all cases, the results of the mass spectrometry measurements are per mass bin. For mass bins in which multiple isobars exist, the fissiogenic ratio based on the simulation results was used to delineate the contribution of the desired isotope to the instrument response. For example, mass bin 150 consisted of ^{150}Nd and the isotope of interest, ^{150}Sm. According to the MCNP simulation results, 58.9% of the mass 150 isobar was attributed to ^{150}Sm and 41.1% to ^{150}Nd. Thus, this fissiogenic ratio is used to estimate the true contribution of ^{150}Sm to the instrument response for mass bin 150. As mentioned in Section 6.2, theoretically a chemical separation technique could be used to isolate the elements of Cs, Nd, and Sm prior to mass spectrometry measurements in order to avoid the need to use fissiogenic ratios.

Table 19: Comparison of fission product masses measured by mass spectrometry and simulated by MCNP. Reprinted with permission from J.M. Osborn *et al*., 2018

Isotopes	Fissiogenic Ratio	Measured Mass (g)	Relative Error in Measured Mass	Simulated Mass (g)	S/E[a]
^{133}Cs	1	5.22×10^{-7}	6.0%	5.42×10^{-7}	1.04
^{135}Cs	1	1.50×10^{-7}	6.2%	1.42×10^{-7}	0.94
^{137}Cs	0.976	5.08×10^{-7}	6.0%	5.14×10^{-7}	1.01
^{148}Nd	0.983	1.55×10^{-7}	5.8%	1.54×10^{-7}	0.99
^{149}Sm	1	8.34×10^{-9}	5.8%	9.51×10^{-9}	1.14
^{150}Sm	0.589	9.22×10^{-8}	5.8%	9.24×10^{-8}	1.00
^{152}Sm	1	5.55×10^{-8}	5.8%	5.58×10^{-8}	1.01
^{153}Eu	1	1.76×10^{-8}	5.9%	1.87×10^{-8}	1.06

[a] S/E = simulation/measurement

Table 19 shows an excellent agreement between the mass spectrometry measured fission product isotope masses and the MCNP predictions, with most isotope measurements with 5% of the predicted mass. Tables 14 through 19 serve to experimentally characterize the natural UO_2 irradiation at MURR, as well as to validate the fission product and actinide predictions resulting from the MCNP simulation of the experimental irradiation at MURR.

9. MAXIMUM LIKELIHOOD ANALYSIS

The final step in meeting the research objective of developing a nuclear forensics reactor-type discrimination methodology which also determines burnup and time since irradiation of the sample, was to perform an experimental validation study. Obtaining experimental measurements of irradiated fuel representative of that produced in various reactor types was the motivation for the fuel irradiations at HFIR and MURR. The two irradiation campaigns resulted in two distinct fuel samples containing weapons-useable plutonium, suitable for testing the reactor-type discrimination methodology developed.

9.1 HFIR Irradiated Measurement Vector

Following completion of the experimental irradiation at HFIR on June 1, 2013, one of the 12.9 mg DUO_2 fuel discs was dissolved and a forensics characterization performed. Results from the forensic characterization concluded that the DUO_2 fuel discs were irradiated to a burnup of 4.36 ± 0.28 GWd/MTU, and the irradiation produced nearly 200 μg of plutonium with 89% ^{239}Pu.[13]

In support of the study presented here, an additional set of mass spectrometry measurements were performed on October 19, 2017 in order to obtain measured values for the intra-element isotope ratios utilized in the maximum likelihood analysis.
Due to a barium contamination in the mass spectrometry data as a result of the tuning solution used by the mass spectrometer, only nine of the ten intra-element isotope ratios were measurable. Table 20 contains the mass spectrometry measured intra-element ratio values for the HFIR irradiated material, as obtained by the procedures detailed in Section 6.2.

Table 20: The mass spectrometry measured intra-element isotope ratios for the HFIR irradiated material.

Ratio	Measured Value	Measurement Error (%)
$^{137}Cs/^{133}Cs$	1.30×10^{0}	6.7
$^{134}Cs/^{137}Cs$	3.74×10^{-3}	4.2
$^{135}Cs/^{137}Cs$	4.25×10^{-1}	10.
$^{154}Eu/^{153}Eu$	4.67×10^{-2}	4.5
$^{150}Sm/^{149}Sm$	3.23×10^{0}	2.7
$^{152}Sm/^{149}Sm$	2.93×10^{0}	1.3
$^{240}Pu/^{239}Pu$	8.28×10^{-2}	0.59
$^{241}Pu/^{239}Pu$	3.30×10^{-2}	0.88
$^{242}Pu/^{239}Pu$	1.88×10^{-3}	0.88

9.2 HFIR Irradiation Maximum Likelihood Analysis Results

Using the measured set of nine intra-element ratios contained in Table 20, the maximum likelihood analysis was performed for the DUO_2 fuel samples experimentally irradiated at HFIR. Table 21 contains the results of the maximum likelihood analysis on the HFIR irradiated material. Each library reactor model is ranked based on the log-likelihood value. Also tabulated is the predicted fuel burnup and time since irradiation corresponding to the maximum log-likelihood value. From Eq. 5 it is evident that the maximum possible log-likelihood value, for a given measurement, will occur when the vector of measured intra-element isotope ratio values perfectly matches with a simulation vector. Thus, the maximum possible log-likelihood value is a function of the simulation uncertainties, $\sigma_{j,sim,}$ if and when the simulation vector is equal to the

measurement vector, $r_{sim} = r_{mes}$. As mentioned in Section 3.3, MCNP does not propagate uncertainties in isotope concentrations through burnup simulations. A 10% simulation error was assumed for the concentration of each isotope. Two isotopes propagated together, a ~14% error was assumed as the ratio uncertainty for each simulated ratio value. With the assumed relative error on the simulation ratio value and the condition $r_{sim} = r_{mes,}$ Eq. 5 calculated the maximum possible log-likelihood value for the HFIR irradiated material as 28.5.

Table 21: Results of the maximum likelihood analysis for the HFIR irradiated material.[a]

Reactor Model	Log-Likelihood Value [b]	Predicted Burnup (GWd/MTU)	Predicted Time Since Irradiation (days)
HFIR [c]	+19.5 ± 4.6	$4.29^{-0.25}_{+0.65}$	1827^{-630}_{+414}
MURR	-46.6 ± 12.8	4.16	1700
NRX	-52.5 ± 12.5	4.13	1590
Magnox	-59.5 ± 13.3	3.00	421
PWR (2.35%)	-86.7 ± 21.0	≥ 5.31	1705
PHWR	-129 ± 32	≥ 4.35	2308
PWR (3.4%)	-284 ± 26	≥ 5.01	0
PWR (4.45%)	$(-5.27 \pm 0.14) \times 10^3$	≥ 3.90	0
FBR	$(-6.39 \pm 0.11) \times 10^5$	≥ 4.73	0

[a] Measured material was HFIR irradiated to a burnup of 4.36 ± 0.28 GWd/MTU with 1601 days decay

[b] The maximum possible log-likelihood value for the measured material is 28.5.

[c] The spread in burnup and time since irradiation predictions was calculated at one standard deviation below the maximum log-likelihood for the most likely reactor model only.

Table 21 shows that the reactor-type discrimination methodology correctly identified the most likely source reactor model for the measured material as the HFIR model, with a log-likelihood value of 19.5 ± 4.6 compared to a maximum possible log-likelihood value of 28.5. The predicted burnup and time since irradiation for the HFIR model corresponding with the maximum log-likelihood value is 4.29 GWd/MTU and 1827 days, respectively, compared to the known burnup of 4.36 ± 0.28 GWd/MTU and known time since irradiation of 1601 days. The predicted burnup and time since irradiation are within 2% and 15% of the known values, respectively. As a reminder, the log-likelihood was calculated via Eq. 5, and the standard deviation in the log-likelihood was calculated via Eq. 9 by propagation of uncertainties. Subtracting one standard deviation (4.6) from the maximum log-likelihood value for the HFIR model (+19.5), the spread in the burnup and time since irradiation predictions can be observed at the log-likelihood value of +14.9. At one standard deviation below the HFIR maximum log-likelihood value, the possible burnup values range from 4.04 to 4.94 GWd/MTU and the possible time since irradiation values range from 1197 to 2241 days. The resulting three-dimensional likelihood surface map and two-dimensional likelihood contour map for the HFIR model (the most likely reactor model in this case) are illustrated in Fig. 30(a) and 30(b), respectively. While the likelihood value for the most likely reactor is seen to follow a Gaussian shape, the reactor models not likely of being the source of the measured material may not have such a shape.

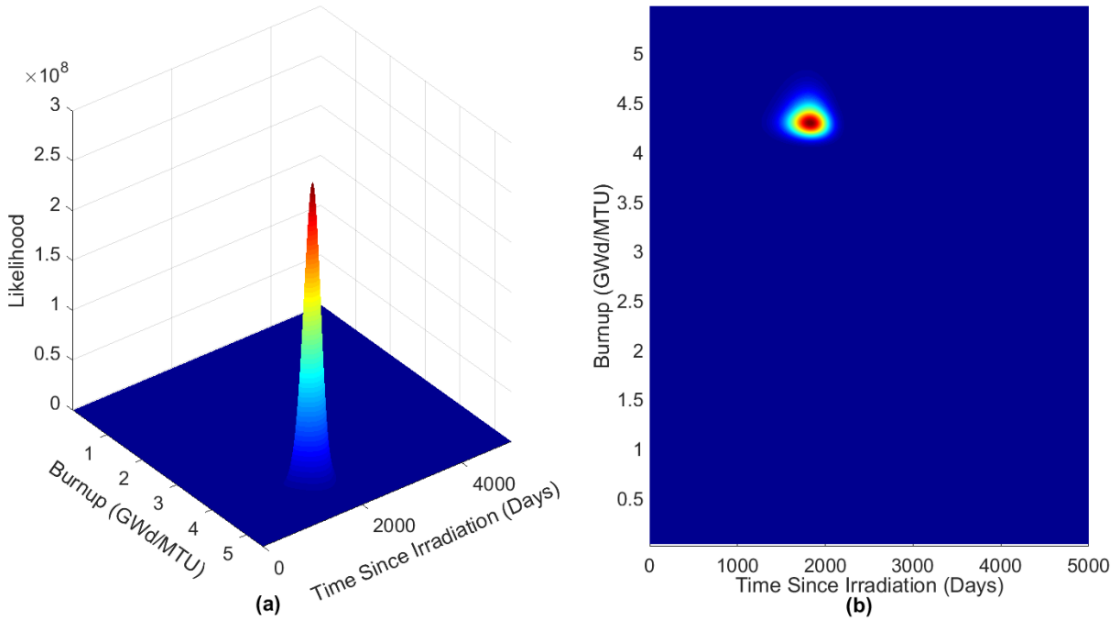

Figure 30: Results of Maximum Likelihood Analysis for the HFIR Irradiated Material (a) 3-D Likelihood Surface Map and (b) 2-D Contour Map for the Most Likely Reactor (HFIR).

The next most likely reactor models are the MURR, NRX, and Magnox models. This is a non-intuitive result as these three models are thermal neutron irradiations. For the MURR and NRX models, the log-likelihood value is poor while the burnup and time since irradiation predictions are fairly accurate. This is due to the selected vector of simulated intra-element ratios having similar values to the measurement vector for ratios which contribute to burnup and time since irradiation predictions, but dissimilar values for the $^{135}Cs/^{137}Cs$, $^{150}Sm/^{149}Sm$, and $^{152}Sm/^{149}Sm$ ratios which depend heavily on thermal neutron flux magnitude and largely contribute to the reactor-type prediction. It should be noted that for the PHWR, FBR, and all three PWR models, the predicted burnup occurs at the maximum burnup level simulated for the respective models.

Therefore, a prediction of this value is interpreted as the most likely point occurring at, or beyond, the boundary of the simulated burnup space. However, based on the log-likelihood values it is evident that the PHWR, FBR, and three PWR models are not the source of the measured material.

Based on the maximum likelihood analysis the FBR model is the least likely source of the HFIR irradiated material. Again, this is a non-intuitive result as the experimental irradiation at HFIR was intended to serve as a surrogate to FBR blanket material. The gadolinium irradiation capsule was utilized to absorb the thermal component of the HFIR neutron flux. However, depletion of neutron-absorbing isotopes of gadolinium (^{152}Gd, ^{155}Gd, and ^{157}Gd) occurred throughout the irradiation. As a result of the depletion of the gadolinium capsule, the fuel discs were exposed to the full (thermal) HFIR neutron flux for the majority of the irradiation after 1 GWd/MTU of burnup was surpassed. Figure 31 displays the 238-energy-group neutron flux, as calculated by MCNP, observed by the DUO_2 fuel discs at the beginning of irradiation and end of irradiation, as well as for the FBR radial blanket. This shows that the flux at the beginning of the HFIR irradiation contained a significant epi-thermal contribution which is not present in an actual FBR blanket neutron flux, and moved even further to a thermal flux throughout the irradiation. For simplicity, the flux at only the beginning and end of irradiation is plotted, however the MCNP simulation showed the flux spectra gradually became more thermal throughout the irradiation. Table 22 contains the values of the neutron flux magnitude the DUO_2 fuel discs were exposed to at the beginning and end of irradiation, indicating that the total neutron flux increased by nearly 50% and the

thermal neutron flux increased by more than two orders of magnitude. In terms of neutron fluence the DUO_2 fuel discs were exposed to a larger thermal neutron fluence than a fast/epi-thermal neutron fluence. The HFIR model simulating the experimental irradiation at HFIR includes the behavior of the gadolinium irradiation capsule depletion and changing neutron flux.

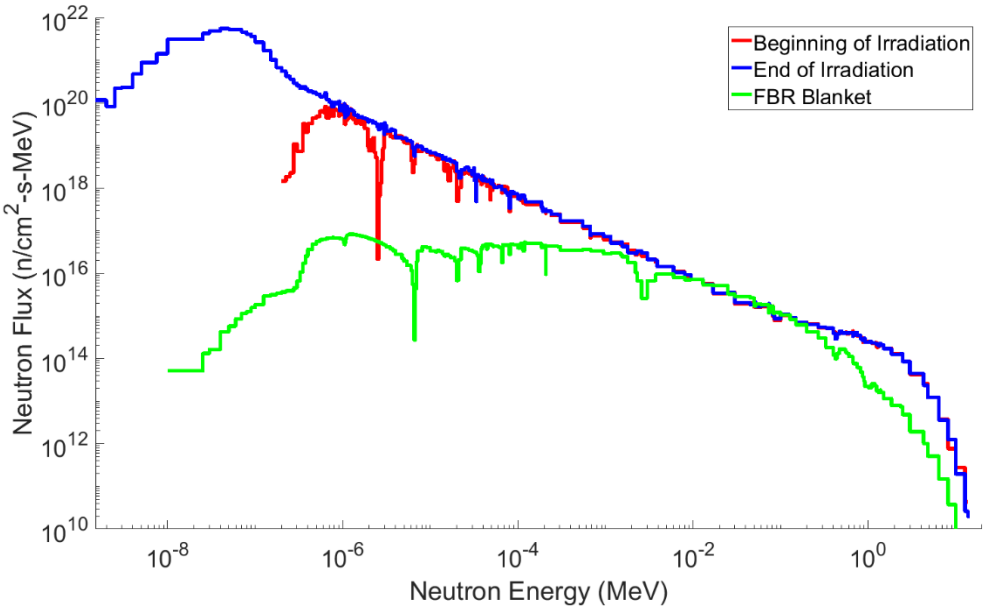

Figure 31: The MCNP calculated 238-energy-group neutron flux per MeV for the experimental irradiation at HFIR at the beginning of irradiation and the end of irradiation, due to the depletion of the gadolinium irradiation capsule, compared to that of the FBR blanket.

Table 22: Comparison of the MCNP calculated neutron flux magnitude at the beginning and end of the experimental irradiation at HFIR.

HFIR Irradiation	Total Flux Magnitude (n/cm^2-s)	Thermal Flux E < 0.5 eV (n/cm^2-s)	Fast Flux E > 0.1 MeV (n/cm^2-s)
Beginning of Irradiation	1.60×10^{15}	5.86×10^{12}	8.03×10^{14}
End of Irradiation	2.36×10^{15}	6.39×10^{14}	8.05×10^{14}

9.3 MURR Irradiated Measurement Vector

On March 9, 2018 mass spectrometry measurements of the MURR irradiated UO_2 material were performed in order to obtain measured values for the intra-element isotope ratios. Again, due to a barium contamination in the mass spectrometry data as a result of the tuning solution used by the mass spectrometer, a measured value for the $^{136}Ba/^{138}Ba$ ratio was unable to be obtained. Additionally, a measured value for the $^{154}Eu/^{153}Eu$ ratio was not obtained as the amount of ^{154}Eu was below the minimum detectable limit via mass spectrometry or gamma spectrometry. Thus, the eight mass spectrometry measured intra-element ratio values are contained in Table 23. The smaller total plutonium concentration in the MURR irradiated material led to larger measurements errors in the plutonium ratios when compared to the HFIR irradiated material shown in Table 20.

Table 23: The mass spectrometry measured intra-element isotope ratios for the MURR irradiated material.

Ratio	Measured Value	Measurement Error (%)
$^{137}Cs/^{133}Cs$	9.75×10^{-1}	6.6
$^{134}Cs/^{137}Cs$	3.84×10^{-3}	7.0
$^{135}Cs/^{137}Cs$	2.95×10^{-1}	6.8
$^{150}Sm/^{149}Sm$	9.88×10^{0}	6.7
$^{152}Sm/^{149}Sm$	6.65×10^{0}	5.7
$^{240}Pu/^{239}Pu$	4.77×10^{-2}	5.7
$^{241}Pu/^{239}Pu$	2.40×10^{-3}	5.8
$^{242}Pu/^{239}Pu$	5.99×10^{-5}	8.3

9.4 MURR Irradiation Maximum Likelihood Analysis Results

Using the measured vector of eight intra-element ratios contained in Table 23, the maximum likelihood analysis was performed for the natural UO_2 fuel samples experimentally irradiated at MURR. Table 24 contains the results of the maximum likelihood analysis on the MURR irradiated material. Each library reactor model is ranked based on the log-likelihood value. As before, the predicted fuel burnup and time since irradiation corresponding to the largest log-likelihood value are also tabulated. The maximum possible log-likelihood value for the MURR irradiated material was calculated as 29.7.

Table 24: Results of the maximum likelihood analysis for the MURR irradiated material.[a]

Reactor Model	Log-Likelihood Value [b]	Predicted Burnup (GWd/MTU)	Predicted Time Since Irradiation (days)
MURR [c]	+29.5 ± 1.1	$1.02^{-0.05}_{+0.03}$	295^{-264}_{+226}
NRX	+25.3 ± 3.0	1.03	208
Magnox	+13.2 ± 5.7	0.73	0
PWR (3.4%)	-6.02 ± 8.71	3.91	1381
PWR (4.45%)	-8.88 ± 10.2	≥ 3.90	1196
PWR (2.35%)	-12.7 ± 10.2	3.10	1202
PHWR	-14.7 ± 13.8	1.02	360
HFIR	-166 ± 28	4.40	1790
FBR	(-1.52 ± 0.20) × 10^5	≥ 4.73	0

[a] Measured material was MURR irradiated to a burnup of 0.973 ± 0.032 GWd/MTU with 318 days decay.
[b] The maximum possible log-likelihood value for the measured material is 29.7.
[c] The spread in burnup and time since irradiation predictions was calculated at one standard deviation below the maximum log-likelihood for the most likely reactor model only.

Table 24 shows that the reactor-type discrimination methodology correctly identified the most likely source reactor model for the measured material as the MURR model, with a log-likelihood value of 29.5 ± 1.1 compared to a maximum possible log-likelihood value of 29.7. The predicted burnup and time since irradiation for the MURR model corresponding with the maximum log-likelihood value is 1.02 GWd/MTU and 295 days, respectively, compared to the known burnup of 0.973 ± 0.032 GWd/MTU and known time since irradiation of 318 days. The predicted burnup and time since irradiation are within 5% and 8% of the known values, respectively. Subtracting one

standard deviation (1.1) from the maximum log-likelihood value for the MURR model (+29.5), the spread in the burnup and time since irradiation predictions can be observed at the log-likelihood value of +28.4. At one standard deviation below the MURR maximum log-likelihood value, the possible burnup values range from 0.97 to 1.05 GWd/MTU and the possible time since irradiation values range from 31 to 521 days. The resulting three-dimensional likelihood surface map and two-dimensional likelihood contour map for the MURR model (the most likely reactor model in this case) are illustrated in Fig. 32(a) and 32(b), respectively.

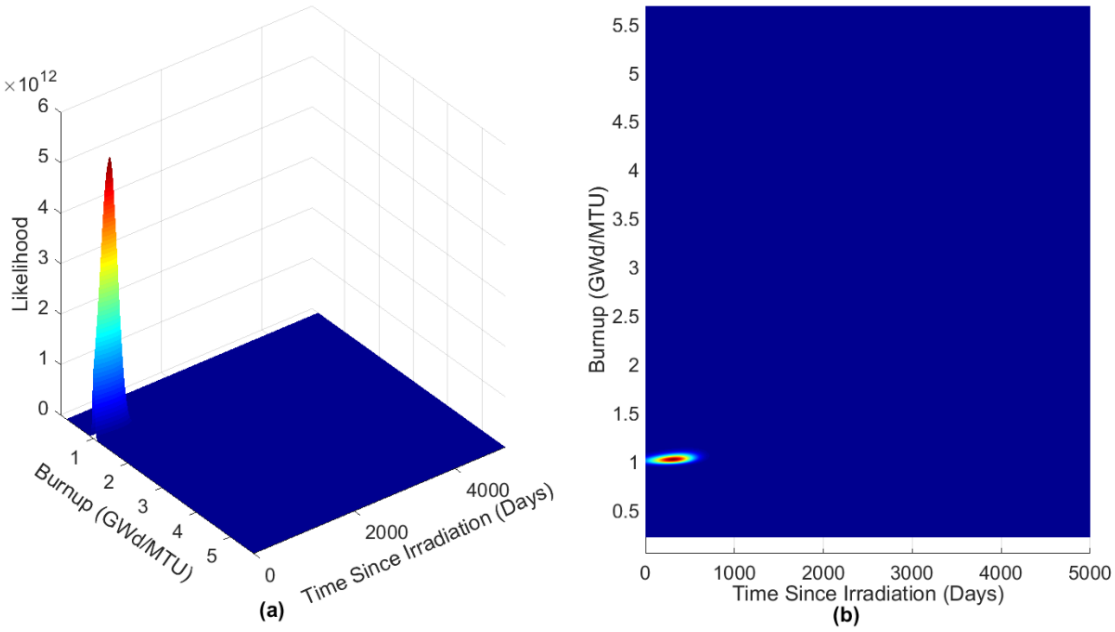

Figure 32: Results of Maximum Likelihood Analysis for the MURR Irradiated Material (a) 3-D Likelihood Surface Map and (b) 2-D Contour Map for the Most Likely Reactor (MURR).

Analyzing the log-likelihood values in Table 24, the reactor models can be categorized into groups. The most likely reactor models are the MURR simulation and the NRX. The difference in the log-likelihood values between the MURR and NRX models is significant to one standard deviation, but within a larger confidence interval the two models are not significantly different. The next most likely reactor type within the library is the Magnox. These results are as expected since the NRX and Magnox are natural uranium fueled thermal reactors, similar to the experimental irradiation at MURR. The PHWR model and three PWR models are grouped together with intermediately low log-likelihood values. It is also evident from the log-likelihood values that neither the fast neutron, FBR model, nor the mixed pseudo-fast to thermal neutron, HFIR model, is the source of the measured material. The maximum likelihood analysis works well for identifying the most likely source reactor model, as well as discriminating against the reactor models which are highly unlikely to be the source reactor type. For reactor models with intermediately low log-likelihood values, the correct interpretation is the reactor operated under the conditions modeled is likely not to be the source of the measured material. Drawing any further conclusions from reactor models with low log-likelihood values may not be appropriate.

9.5 Further Discussion of Maximum Likelihood Results

The maximum likelihood results correctly identified the source reactor model for both experimentally irradiated test cases. For the HFIR irradiated material case the HFIR model resulted in a log-likelihood value of 19.5 ± 4.6 compared to a maximum possible log-likelihood value of 28.5. The maximum log-likelihood value does lie within three

standard deviations of the HFIR model log-likelihood value. However, the maximum likelihood analysis for HFIR irradiated material case appears to not have performed as well when compared to the MURR irradiated material case.

This could be due to the difficulty in the MCNP simulation to capture the behavior of the complex HFIR irradiation. For both analyses, a 10% simulation error was assumed for the concentration of each isotope in the ratio. However, by propagating the reaction rate errors in the MCNP simulations for total fission and total plutonium production, it is evident that the HFIR simulation has larger stochastic uncertainties than the MURR simulation. For the MURR simulation the stochastic relative error in the total fissions, which is synonymous with the predicted ^{137}Cs concentration, is 0.086%, and the stochastic relative error in the predicted plutonium mass is 0.781%. Conversely for the HFIR simulation, the stochastic relative error in the predicted ^{137}Cs concentration is 0.395%, and the stochastic relative error in the predicted plutonium mass is 6.91%. Clearly the errors in the simulated intra-element isotope ratios for the HFIR model will be larger than the errors in the simulated ratios for the MURR model. This likely led to the HFIR model not agreeing as well with the measured ratios.

A study by Garcia-Herranz *et al.*[57] found that when a sufficient number of histories are simulated in a Monte Carlo calculation, the statistical errors are negligible compared to the systematic errors such as cross-section uncertainties. As a result, it is expected that the difference in the total errors (systematic and stochastic) of the isotope concentrations for the HFIR and MURR simulations will not be as significant as the nearly order of magnitude difference in the stochastic errors. In order to assess how the

HFIR irradiated material maximum likelihood results would vary with increasing simulation error, the analysis was performed with 15% and 20% assumed errors on each isotope concentration. Table 25 displays the log-likelihood values when a simulated isotope concentration error of 10%, 15%, and 20% was assumed. The burnup and time since irradiation predictions do change with the varying simulation error, but not significantly.

Table 25: Log-Likelihood results of the maximum likelihood analysis for the HFIR irradiated material at various levels of simulation error.

Reactor Model	Log-Likelihood Value (10% Simulation Error)	Log-Likelihood Value (15% Simulation Error)	Log-Likelihood Value (20% Simulation Error)
Maximum Possible Log-Likelihood	**28.5**	**24.9**	**22.3**
HFIR	+19.5 ± 4.6	+20.7 ± 2.9	+19.9 ± 2.2
MURR	-46.6 ± 12.8	-11.1 ± 8.2	+0.1 ± 6.1
NRX	-52.5 ± 12.5	-14.7 ± 8.3	-2.7 ± 6.2
Magnox	-59.5 ± 13.3	-18.0 ± 8.7	-4.7 ± 6.5
PWR (2.35%)	-86.7 ± 21.0	-26.5 ± 12.0	-6.8 ± 8.4
PHWR	-129 ± 32	-53.3 ± 18.2	-23.2 ± 11.9
PWR (3.4%)	-284 ± 26	-114 ± 17	-56.1 ± 12.7
PWR (4.45%)	$(-5.27 \pm 0.14) \times 10^3$	$(-2.33 \pm 0.08) \times 10^3$	$(-1.30 \pm 0.06) \times 10^3$
FBR	$(-6.39 \pm 0.11) \times 10^5$	$(-2.84 \pm 0.05) \times 10^5$	$(-1.60 \pm 0.03) \times 10^5$

The log-likelihood equation is based on distinguishing the differences between the measurement intra-element isotope ratio set and the simulation ratio set. A small simulation error serves to exacerbate the differences between the measurement and

simulation ratio sets, while a large simulation error lessens the discrepancy. Thus, as the simulation error increases the log-likelihood equation becomes less effective at discriminating between the measurement set and simulation sets. This general behavior is observed in Table 25. As the simulation error is increased the HFIR model log-likelihood value approaches that of the maximum possible log-likelihood value. However, the incorrect reactors also become closer to the maximum log-likelihood value, and the log-likelihood has less of an ability to discriminate amongst the incorrect reactor-type models. This highlights the need to use appropriate simulated ratio errors which account for stochastic and systematic uncertainties.

In this study, the measurement errors on the measured intra-element isotope ratio values ranged on the order of 5% to 10%. The measurement errors did not seem to negatively affect the analysis, indicating 5-10% measurement errors are completely adequate.

10. CONCLUSIONS

The objective of this research was to develop a nuclear forensics methodology that is capable of source reactor-type discrimination of chemically separated weapons-usable plutonium. If special nuclear material is interdicted, a few steps may be followed leading to the utilization of the methodology developed through this study. The first step will be to perform a gamma spectrometry measurement to ascertain whether the material contains plutonium. Next, a sample will be drawn to perform precise gamma and mass spectrometry measurements to obtain fission product and plutonium intra-element isotope ratios. Ideally, as many intra-element isotope ratios as possible would be measured, however this work has shown eight or nine measured ratios is sufficient. Subsequently, the measured intra-element isotope ratios can be utilized in the nuclear forensics methodology for discriminating against reactor types not likely of being the source of the interdicted material. The information gained by the reactor-type discrimination methodology, when combined with traditional forensics, may enable attribution of the plutonium.

The developed methodology utilizes intra-element isotope ratios of fission products and plutonium in order to be insensitive to a possible chemical separation. The list of identified intra-element isotope ratios for the methodology to predict information on reactor type, burnup, and time since irradiation of the sample ended includes: $^{137}Cs/^{133}Cs$, $^{134}Cs/^{137}Cs$, $^{135}Cs/^{137}Cs$, $^{136}Ba/^{138}Ba$, $^{150}Sm/^{149}Sm$, $^{152}Sm/^{149}Sm$, $^{154}Eu/^{153}Eu$, $^{240}Pu/^{239}Pu$, $^{241}Pu/^{239}Pu$, and $^{242}Pu/^{239}Pu$. The MCNPX-2.7 and MCNP6 radiation transport codes were used to model reactor cores, perform burnup simulations, and

estimate the isotopics of the discharged fuel. The simulation results were used to generate a reactor-dependent library of the identified intra-element isotope ratio values as a function of burnup and time since irradiation. The maximum likelihood formulation contained in the nuclear forensics methodology was utilized to compare the simulated intra-element isotope ratio values contained in the reactor library to the same ratio values measured in the sample. This approach results in a likelihood value which is proportional to the probability of observing the measured intra-element isotope ratios given the reactor type and parameters.

An ideal demonstration of the developed nuclear forensics methodology was to perform a validation study by testing the methodology with measurements of weapons-usable plutonium. In addition, the weapons-usable plutonium should be representative of plutonium which would be produced in a realistic production reactor. In order to allow such a validation study of the methodology, two experimental irradiation campaigns were performed, resulting in two distinct fuel samples containing weapons-useable plutonium. To replicate weapons-usable plutonium produced in the blanket of a fast breeder reactor, DUO_2 fuel samples were irradiated within the HFIR facility using a gadolinium capsule to replicate a pseudo-fast neutron spectrum. A characterization of the experimental irradiation at HFIR and resulting plutonium was previously performed by Swinney,[13] however the current study led to a more thorough understanding of the behavior of the gadolinium irradiation capsule and changing neutron flux.

The second irradiation campaign was designed to produce weapons-usable plutonium which is consistent with the low burnup material from natural uranium fueled

thermal neutron reactors. Three natural UO_2 fuel discs with an average mass of 16.46 mg were irradiated in the graphite reflector region surrounding the MURR core. A detailed MCNP model was developed for simulating the experimental irradiation ta MURR. Comparisons of the MCNP burnup simulation results for the experimental irradiation at MURR to the PHWR, NRX, and Magnox–type reactors confirmed that the experimental irradiation was successful in producing surrogate material consistent with low burnup material from a natural uranium fueled thermal neutron reactor. The majority of the MCNP-predicted plutonium and fission product isotope concentrations matched within 10% of the measured sample concentrations.

Next, the irradiated UO_2 samples were subjected to nondestructive and destructive analyses to characterize the irradiation at MURR and the plutonium produced. The gamma-spectrometry-measured activities provided data on multiple radioactive fission product isotopes within the irradiated fuel. The measured ^{137}Cs activity was used to calculate that the irradiated fuel discs attained a burnup of 0.973 ± 0.032 GWd/MTU. The suite of gamma and mass spectrometry measured fission product concentrations showed excellent agreement with the simulation, and served to verify the fission product concentration predictions from the MCNP burnup simulation of the experimental irradiation at MURR.

Mass spectrometry measurements of the irradiated samples showed acceptable agreement with MCNP simulation predictions regarding the quantity and quality of plutonium produced. The results of the simulation and mass spectrometry both conclude that the irradiation successfully produced weapons-usable plutonium. It was calculated

by mass spectrometry that 20.1 μg of plutonium was produced within the dissolved fuel disc, 95.22% of which was ^{239}Pu.

Ultimately, having acquired two distinct, well-characterized, fuel samples containing weapons-usable plutonium, mass spectrometry measurements were performed on both experimentally irradiated samples in order to obtain measured values for the intra-element isotope ratios employed by the maximum likelihood analysis of the nuclear forensics methodology. Measured values of nine intra-element isotope ratios were obtained for the material which was experimentally irradiated at HFIR, and measured values of eight intra-element isotope ratios were obtained for the material which was experimentally irradiated at MURR.

The results of the maximum likelihood analysis for the measured HFIR irradiated material, which underwent a complex irradiation due to the gadolinium depletion and significantly changing neutron flux, showed that the reactor-type discrimination methodology correctly identified the HFIR model as the source reactor type. The maximum log-likelihood value for the HFIR model was 19.5 ± 4.6 compared to a maximum possible log-likelihood value of 28.5. The predicted burnup was within 2% of the known burnup of 4.36 ± 0.28 GWd/MTU, and the predicted time since irradiation was within 15% of the known 1601 days.

The results of the maximum likelihood analysis for the measured MURR irradiated material showed that the reactor-type discrimination methodology correctly identified the MURR model as the source reactor type. The maximum log-likelihood value for the MURR model was 29.5 ± 1.1 compared to a maximum possible log-

likelihood value of 29.7. The predicted burnup was within 5% of the known burnup of 0.973 ± 0.032 GWd/MTU, and the predicted time since irradiation was within 8% of the known 318 days.

In conclusion, the reactor-type discrimination methodology utilizing maximum likelihood analysis works well for discriminating against reactor types not likely to be the source of the measured material. Given the source reactor is contained within the reactor library, the methodology works to identify the source reactor model. The methodology also works well for predicting the burnup and time since irradiation of the measured material when a likely reactor is identified. The methodology performed as expected for both experimentally irradiated cases, identifying the source reactor model and predicting the parameters of burnup and time since irradiation. The two experimental irradiation cases included variations in the fuel sample enrichment, neutron flux shape and magnitude, level of sample burnup, and duration of time since irradiation. The research presented here served to develop and experimentally validate a nuclear forensics reactor-type discrimination methodology.

10.1 Journal Publications Resulting from this Study

1. S.S. CHIRAYATH, J.M. OSBORN, T.M. COLES, “Trace Fission Product Ratios for Nuclear Forensics Attribution of Weapons-Grade Plutonium From Fast and Thermal Reactors,” *Sci. & Global Secur.*, 23, 48–67, (2015). doi:10.1080/08929882.2015.996079
2. J.M. OSBORN, E.D. KITCHER, J.D. BURNS, C.M. FOLDEN III, S.S. CHIRAYATH, “Nuclear Forensics Methodology for Reactor-Type Attribution of

Chemically Separated Plutonium," *Nucl. Technol.*, 201, 1-10 (2017). doi:10.1080/00295450.2017.1401442.

3. J.M. OSBORN, K.J. GLENNON, E.D. KITCHER, J.D BURNS, C.M. FOLDEN III, S.S. CHIRAYATH, "Computational and Experimental Forensics Characterization of Weapons-grade Plutonium Produced in a Thermal Neutron Environment," *Nucl. Eng. Technol.*, 50, 820-828 (2018). doi:10.1016/j.net.2018.04.017.
4. J.M. OSBORN, K.J. GLENNON, E.D. KITCHER, J.D BURNS, C.M. FOLDEN III, S.S. CHIRAYATH, "Experimental Validation of a Nuclear Forensics Methodology for the Source Reactor-Type Discrimination of Chemically Separated Plutonium," *Nucl. Eng. Technol.*, Under Review.
5. E.D. KITCHER, J.M. OSBORN, K.J. GLENNON, C.M. FOLDEN III, S.S. CHIRAYATH, "Sensitivity Studies on a Novel Forensics Methodology for Source Reactor-Type Characterization of Separated Weapons Grade Plutonium," In preparation.

10.2 Future Work

The most pertinent future improvement to this research would be to quantify the intra-element isotope ratio simulation uncertainties propagated through multiple transport-depletion steps in MCNP burnup calculations. As part of this research we have identified a framework for manually propagating the reaction rates and errors through each time step for the reactions which significantly contribute to the production and loss of an isotope. The framework was demonstrated for the isotope ^{137}Cs. This provides the

ability to estimate the stochastic error in the Monte Carlo calculation, but does not account for systematic errors. The simulation errors have an effect on the performance of the maximum likelihood analysis, thus it will be advantageous to have appropriate estimations of the simulated ratio errors including stochastic and systematic uncertainty contributions.

For both the measurement ratio values and simulation ratio values, it is understood that the values come from a distribution. The log-likelihood equation utilized in this work compares the mode of the measurement to the mode of the simulation and provides a quantitative value on the difference between the two modes. The standard deviation in the simulation ratio distribution is used for weighting the log-likelihood (Eq. 5) whereas the standard deviations in the simulation ratio and measurement ratio distributions are used in estimating error propagation in the log-likelihood (Eq. 9). As can be seen in Table 25, a variation in the simulation errors has an effect on the magnitude of the log-likelihood values, but it does not have an effect on the ranking of the reactors or predicted parameters. Given that the modes do not change, the ranking order of reactors, predicted burnup, and predicted time since irradiation will not change. Future work could examine the use of method which compares two distributions, such as the Bhattacharyya coefficient methods. By appropriately sampling the measurement and simulation distributions, and thus fluctuating the modes, the measurement and simulation errors may lead to variations in the reactor ranking and predicted parameters.

Next, efforts should be made to expand the reactor library to include high-fidelity models of as many reactor types as possible. Furthermore, identification of additional

intra-element isotope ratios will be needed to expand the reactor parameter space to include variables such as initial fuel enrichment, thermal neutron flux magnitude, power level, etc.

Additionally, the sensitivity of the reactor-type discrimination methodology and the associated burnup and time since irradiation parameter predictions should be analyzed with respect to a reduced number of measured isotope ratio values. In the case that not all ten intra-element isotope ratios are measureable, a subset of isotope ratios may be more important at predicting the parameters of interest. This subset will be case-specific as well as being dependent on which parameters are more important to be resolved.

Finally, by overlaying the reactor-type discrimination methodology with a database of reactor operation history which includes information such as reactor type, cycle burnups, and cycle dates, a step could be taken towards reactor attribution. A measured sample will result in the maximum likelihood identifying the most likely reactor type, and predicting the burnup and time since irradiation. Theoretically, these predictions would be used to search the database to identify a specific reactor of the predicted type that has a known fuel cycle with parameters matching the burnup and time since irradiation predictions. Such a reactor operation history database could be populated by reactor operator declarations or opens source information such as satellite imagery.

REFERENCES

1. United States Department of Defense, Office of the Secretary of Defense, *Nuclear Posture Review, 2018*, (2018).

2. K.J. MOODY, I. HUTCHEON, and P.M. GRANT, *Nuclear Forensics Analysis*, Taylor & Francis Group, Boca Raton, Fla, (2005).

3. World Nuclear Association, *Safeguards to Prevent Nuclear Proliferation*, (2017), http://www.world-nuclear.org/information-library/safety-and-security/non-proliferation/safeguards-to-prevent-nuclear-proliferation.aspx.

4. M. MILLER, "NUCLEAR ATTRIBUTION AS DETERRENCE," *Nonproliferation Review*, 14:1, 33-60 (2007). doi:10.1080/10736700601178465.

5. B. VOLDERS, T. SAUCER, *Nuclear Terrorism: Countering the threat*, Routledge, New York (2016).

6. M. WALLENIUS, P. PEERANI, L. KOCH, "Origin Determination of Plutonium Material in Nuclear Forensics," *J. Radioanal. Nucl. Ch.*, 246, 317-321 (2000). doi:10.1023/A:1006774524272.

7. J.C. MARK, "Explosive Properties of Reactor-Grade Plutonium," *Sci. and Global Secur.*, 4, 111-128 (1993). doi:10.1080/08929889308426394.

8. M.R. STERNAT, "Development of Technical Nuclear Forensics for Spent Research Reactor Fuel." Doctoral dissertation, Texas A&M University, College Station, TX (2012). http : / /hdl .handle .net /1969 .1 /148202.

9. M.R. SCOTT, "Nuclear Forensics: Attributing the Source of Spent Fuel Used in an RDD Event," Master's thesis, Texas A&M University, College Station, TX (2005). http://hdl.handle.net/1969.1/2368.

10. S.S. CHIRAYATH, J.M. OSBORN, T.M. COLES, "Trace Fission Product Ratios for Nuclear Forensics Attribution of Weapons-Grade Plutonium From Fast and Thermal Reactors," *Sci. & Global Secur.*, 23, 48–67, (2015). doi:10.1080/08929882.2015.996079

11. A.E. JONES, P. TURNER, C. ZIMMERMAN, J.Y. GOULERMAS, "Classification of Spent Reactor Fuel for Nuclear Forensics," *Anal. Chem.*, 86:11, 5399-5405 (2014). doi:10.1021/ac5004757.

12. M. ROBEL, M.J. KRISTO, "Discrimination of source reactor type by multivariate statistical analysis of uranium and plutonium isotopic concentrations in unknown irradiated nuclear fuel material," *J. Environ. Radioactiv.*, 99, 1789-1797 (2008). doi:0.1016/j.jenvrad.2008.07.004.

13. M.W. SWINNEY, C.M. FOLDEN III, R.J. ELLIS, S.S. CHIRAYATH, "Experimental and Computational Forensics Characterization of Weapons-grade Plutonium Produced in a Fast Reactor Neutron Environment", *Nucl. Technol.*, 197, 1-11 (2017). doi:10.13182/NT16-76.

14. M.W. SWINNEY, "Experimental and Computational Assessment of Trace Nuclide Ratios in Weapons Grade Plutonium for Nuclear Forensics Analysis" Doctoral dissertation, Texas A&M University, College Station, TX (2015). http://hdl.handle.net/1969.1/156480.

15. P.D. WILSON, *The Nuclear Fuel Cycle: From Ore to Waste*, Oxford University Press, New York, (2001).

16. M. BENEDICT, T. H. PIGFORD, and H. W. LEVI, *Nuclear Chemical Engineering*, Second Edition, McGraw-Hill Series in Nuclear Engineering, New York, (1981).

17. P.M. MENDOZA, S.S. CHIRAYATH, C.M. FOLDEN III, "Fission Product Decontamination Factors for Plutonium Separated by PUREX From Low-Burnup, Fast-Neutron Irradiated Depleted UO_2," *Appl. Radiat. Isotopes*, 118, 38-42 (2016). doi:10.1016/j.apradiso.2016.08.021.

18. I. LANTZOS, C. KOUVALAKI, G. NICOLAOU, "Plutonium fingerprinting in nuclear forensics of spent nuclear fuel," *Prog. Nucl. Energ.*, 85, 333-336 (2015). doi:10.1016/j.pnucene.2015.07.002.

19. A. GLASER, "Isotopic Signatures of Weapon-Grade Plutonium from Dedicated Natural Uranium-Fueled Production Reactors and Their Relevance for Nuclear Forensics Analysis," *Nucl. Sci. Eng.*, 163, 26-33 (2009). doi:10.13182/NSE163-26.

20. *Scale: A comprehensive modeling and simulation suite for nuclear safety analysis and design*, Version 6.1, ORNL/TM-2005/39, (2011).

21. J.F. BRIESMEISTER, Editor, *MCNP – A General Monte Carlo N-Particle Transport Code*, Version 4C, LA-13709-M, (2000).

22. A. G. CROFF, "ORIGEN2: A Versatile Computer Code for Calculating the Nuclide Compositions and Characteristics of Nuclear Materials," *Nucl. Technol.*, 62, 335-352 (1983). doi:10.13182/NT83-1.

23. W.S. CHARLTON, B.L. FEAREY, C.W. NAKHLEH, T.A. PARISH, R.T. PERRY, J. POTHS, J.R. QUAGLIANO, W.D. STANBRO, W.B. WILSON, "Operator declaration verification technique for spent fuel at reprocessing facilities," *Nucl. Instrum. Meth. B,* 168, 98-108 (2000). doi:10.1016/S0168-583X(99)00633-3.

24. C. BRAUN, S. HECKER, C. LAWRENCE, P. PAPADIAMANTIS, *North Korean Nuclear Facilities After the Agreed Framework*, Center for International Security and Cooperation, Stanford University, (2016). http://cisac.fsi.stanford.edu/sites/default/files/khucisacfinalreport_compressed.pdf.

25. P.M. Lee, *Bayesian Statistics: An Introduction*, Fourth Edition, John Wiley & Sons Ltd, West Sussex, UK, (2012).

26. T.L. BURR, W.S. CHARLTON, C.W. NAKHLEH, "Assessing confidence in inferring reactor type and fuel burnup: A Markov chain Monte Carlo approach", *Nucl. Instrum. Meth. A*, 555, 426-434 (2005). doi:10.1016/j.nima.2005.09.041.

27. D.B. PELOWITZ, Editor, *MCNPX User's Manual*, Version 2.7.0, LA-CP-11-00438, (2011).

28. D.B. PELOWITZ, Editor, *MCNP6 User's Manual*, Version 1.0, LA-CP-13-00634, (2013).

29. L.L. CARTER, E.D. CASHWELL, "*Particle-Transport Simulation with the Monte Carlo Method*," Los Alamos Scientific Laboratory, (1975). doi:10.2172/4167844.

30. X-5 Monte Carlo team, *MCNP – A general Monte Carlo N-Particle transport code*, Version 5, LA-UR-03-1987, (2005).

31. M. FENSIN, "Development of the MCNPX Depletion Capability: A Monte Carlo Linked Depletion Method That Automates the Coupling Between MCNPX and CINDER90 for High Fidelity Burnup Calculations," Doctoral dissertation, University of Florida, Gainesville, FL (2008). http://ufdcimages.uflib.ufl.edu/UF/E0/02/19/46/00001/fensin_m.pdf.

32. J. HENDRICKS, G. MCKINNEY, M. FENSIN, M. JAMES, R. JOHNS, J. DURKEE, J. FINCH, D. PELOWITZ, L. WATERS, M. JOHNSON, F. GALLMEIER, *MCNPX 2.6.0 Extensions*, LA-UR-08-2216, (2008).

33. S.C. CHETAL, V. BALASUBRAMANIYAN, P. CHELLAPANDI, P. MOHANAKRISHNAN, P. PUTHIYAVINAYAGAM, C.P. PILLAI, S. RAGHUPATHY, T.K. SHANMUGHAM, C.S. PILLAI, "The Design of the Prototype Fast Breeder Reactor," *Nucl. Eng. Des.*, 236, 52–860 (2006). doi:10.1016/j.nucengdes.2005.09.025.

34. S.S. CHIRAYATH, G. HOLLENBECK, J. RAGUSA, P. NELSON, "Neutronic and Nonproliferation Characteristics of (PuO_2-UO_2) and (PuO_2-ThO_2) as Fast Reactor Fuels," *Nucl. Eng. Des.*, 239, 1916-1924 (2009). doi:10.1016/j.nucengdes.2009.05.019.

35. A. GLASER, M.V. RAMANA, "Weapon-Grade Plutonium Production Potential in the Indian Prototype Fast Breeder Reactor," *Sci. and Global Secur.*, 15, 85-105 (2007). doi:10.1080/08929880701609154.

36. First Atomic Energy of Canada Limited, *Canada Enters the Nuclear Age: A Technical History of Atomic Energy of Canada Limited as Seen from Its Research Laboratories*, McGill-Queen's Press, Montreal, (1997).

37. S.E. JENSEN, E. NONBOL, *Description of the Magnox Type of Gas Cooled Reactor (MAGNOX)*, NKS/RAK-2(97)TR-C5, Riso National Laboratory, (1998).

38. A. AHMAD, A. GLASER, "A Conversion Proposal for Iran's IR-40 Reactor with Reduced Plutonium Production," *Sci. Global Secur.*, 23, 3-19 (2015). doi:10.1080/08929882.2015.996074.

39. D. ALBRIGHT, *Israel's Military Plutonium Inventory*, Institute for Science and International Security, (2015). https://isis-online.org/uploads/isis-reports/documents/Israel_Military_Plutonium_Stock_November_19_2015_Final.pdf.

40. D. ALBRIGHT, S. KELLEHER-VERGANTINI, *India's Stocks of Civil and Military Plutonium and Highly Enriched Uranium, End 2014*, Institute for Science and International Security, (2015). https://isis-online.org/uploads/isis-reports/documents/India_Fissile_Material_Stock_November2_2015-Final.pdf.

41. T. PATTON, “Combining Satellite Imagery and 3D Drawing Tools for Nonproliferation Analysis: A Case Study of Pakistan's Khushab Plutonium Production Reactors,” *Sci. Global Secur.*, 20, 117-140 (2012). doi:10.1080/08929882.2012.719383.

42. N. VEERARAGHAVAN, *Research Reactor Dhruva*, IAEA-SM-310/114, Bhabha Atomic Research Centre. http://www.iaea.org/inis/collection/NCLCollectionStore/_Public/22/047/22047730.pdf.

43. R.S. KEMP, “Two Methods for Converting a Heavy-Water Research Reactor to Use Low-Enriched-Uranium Fuel to Improve Proliferation Resistance After Startup”, *Energy Technology & Policy*, 2:1, 39-46 (2015). doi:10.1080/23317000.2015.1012687.

44. D. ALBRIGHT, C. WALROND, *Update on the Arak Reactor*, Institute for Science and International Security, (2013). https://isis-online.org/uploads/isis-reports/documents/Arak_complex_15July2013.pdf.

45. EEAS Press Team, *Statement of the High Representative/Vice President Federica Mogherini on the conclusion of an Official Document regarding the modernisation of the Arak reactor in Iran*, (2016). http://eeas.europa.eu/archives/docs/statements-eeas/docs/151122_arak_official_document_en.pdf.

46. E. RAUCH, “Development of a Safeguards Approach for a Small Graphite Moderated Reactor and Associated Fuel Cycle Facilities”, Master’s Thesis, Texas A&M University, College Station, TX (2009). http://hdl.handle.net/1969.1/ETD-TAMU-2009-05-739.

47. S.S. BAJAJ, A.R. GORE, "The Indian PHWR," *Nucl. Eng. Des.*, 236, 701-722 (2006). doi:10.1016/j.nucengdes.2005.09.028

48. WESTINGHOUSE ELECTRIC COMPANY LLC, *AP1000 European Design Control* Document: 4.3, (2009). http://www.westinghousenuclear.com/Portals/5/Documents/documentation%20pdfs/Chapter%204%20Section%203.pdf.

49. N. XOUBI, R.T. PRIM III, *Modeling of the High Flux Isotope Reactor Cycle 400*, ORNL/TM-2004/251, Oak Ridge National Laboratory, (2005). https://neutrons.ornl.gov/sites/default/files/modeling_hfir_cycle_400.pdf.

50. Missouri University Research Reactor (MURR): *Safety Analysis Report*, MU Project # 000763, (2006). https://www.nrc.gov/docs/ML0921/ML092110573.pdf.

51. WWW Table of Radioactive Isotopes, (2018), http://nucleardata.nuclear.lu.se/toi/nuclide.asp?iZA=630152.

52. N.N. Greenwood, A. Earnshaw, *Chemistry of the Elements (2nd edition)*, Elsevier, Oxford (1997).

53. International Atomic Energy Agency, *Neutron Fluence Measurements*, STI/DOC/10/107, (1970). http://www.iaea.org/inis/collection/NCLCollectionStore/_Public/34/065/34065175.pdf.

54. A.C. HAYES, G. JUNGMAN, "Determining reactor flux from xenon-136 and cesium-135 in spent fuel," *Nucl. Instrum. Meth. A*, 690, 68-74 (2012). doi:10.1016/j.nima.2012.06.031.

55. DOE Fundamentals Handbook: *Nuclear Physics and Reactor Theory: Volume 2 of 2*, DOE-HDBK-1019/2-93, U.S. Department of Energy, (1993).

56. International Atomic Energy Agency Nuclear Data Services, *Cumulative Fission Yields*, (2018), https://www-nds.iaea.org/sgnucdat/c3.htm#92-U-235.

57. N. GARCIA-HERRANZ, O. CABELLOS, J. SANSZ, J. JUAN, J. KUIJPER, "Propagation of statistical and nuclear data uncertainties in Monte Carlo burn-up calculations," *Annals of Nuclear Engineering*, 35, 714-730 (2008). doi:10.1016/j.anucene.2007.07.022.

Supplemental Sources Consulted

58. J.M. OSBORN, E.D. KITCHER, J.D. BURNS, C.M. FOLDEN III, S.S. CHIRAYATH, "Nuclear Forensics Methodology for Reactor-Type Attribution of Chemically Separated Plutonium," *Nucl. Technol.*, 201, 1-10 (2017). doi:10.1080/00295450.2017.1401442.

59. J.M. OSBORN, K.J. GLENNON, E.D. KITCHER, J.D BURNS, C.M. FOLDEN III, S.S. CHIRAYATH, "Computational and Experimental Forensics Characterization of Weapons-grade Plutonium Produced in a Thermal Neutron Environment," *Nucl. Eng. Technol.*, 50, 820-828 (2018). doi:10.1016/j.net.2018.04.017.